

Research Article

A novel *in-situ* field-assisted powder bed laser fusion using liquid metal enabling microstructure control and strength enhancement of austenitic steel



Xiaoyu Liang ^{a,b,1,*} , Yurong Wang ^{a,c,1} , Wei Liu ^a, Buwei Xiao ^a, Qingze Liu ^a, Yizhuo Sun ^a , Pengcheng Lv ^d, Huabei Peng ^c , Jun Zhou ^d, Lei Zhang ^{a,b}, Feng Lin ^{a,b,**}

^a Department of Mechanical Engineering, Tsinghua University, Beijing 100084, China

^b State Key Laboratory of Clean and Efficient Turbomachinery Power Equipment, Tsinghua University, Beijing 100084, China

^c School of Mechanical Engineering, Sichuan University, Chengdu 610065, China

^d School of Mechanical Engineering, Guangxi University, Nanning, 530004, China

ARTICLE INFO

Keywords:

Austenitic stainless steels
Laser powder bed fusion
Field-assisted process
Mechanical property
Deformation mechanism

ABSTRACT

The layer-by-layer powder bed additive manufacturing approach, which encapsulates the workpiece in powder during processing, imposes limitations on the integration of *in-situ* field assistance and enhances production costs. In this work, a novel laser powder bed fusion has been proposed in which the layer-wise accumulated powder bed is replaced by a thin powder layer floating on the liquid Sn. Such a liquid-metal-assisted laser powder bed fusion presents unique advantages: the characteristic thermal history of deposited materials due to high thermal conductivity and fluidity of liquid metals provides greater possibilities for microstructure modulation; the recyclable liquid metal also reduces the need for powder in the forming cylinder and reduces the number of times the powder is reused. Based on the normalized process diagram of liquid-metal-assisted laser powder bed fusion, forming experiments were carried out on the austenitic stainless steels, and the mechanisms underlying the regulation of fine-grain regions were investigated, along with an analysis of the microstructure of this region. Results indicated that the high cooling rate during liquid-metal-assisted laser powder bed fusion led to a finer microstructure and a heterogeneous grain structure ranging from submicron to micron scales in the austenitic stainless steels. The formed heterogeneous austenitic steel exhibits a yield strength surpassing 1.1 GPa and a tensile strength of 1.5 GPa, while retaining an average uniform elongation of 7 %. The *in-situ* heat treatment principles using liquid metal demonstrated in this work have significant applicability across various additive manufacturing processes and precipitation-hardening alloys.

1. Introduction

Laser powder bed fusion (L-PBF), an additive manufacturing technique, represents a revolutionary technology that offers significant flexibility in the design and processing of materials [1]. Even more promising is that the metallurgical process of L-PBF typically involves multiple cycles of rapid melting and solidification, which creates numerous opportunities to optimize the microstructure and, consequently, the mechanical properties [2,3]. Zheng et al. [4] demonstrated that the melt pool undergoes rapid quenching effects in the initial

deposition stage, resulting in very high cooling rates, followed by multiple cycles of intrinsic heat treatment (IHT) due to repeated laser reheating.

Enhancing the design and control capabilities of the L-PBF process for material microstructure is key to achieving precise formation of complex, heterogeneous structures in parts [5]. The intricate combination of control parameters in the L-PBF process influences the melt pool and solidification dynamics, while newly introduced methods continue to impact the process. Chen et al. [6] and Tan et al. [7] have presented recent advances in field-assisted metal additive manufacturing methods,

* Corresponding author. Department of Mechanical Engineering, Tsinghua University, Beijing 100084, China.

** Corresponding author. Department of Mechanical Engineering, Tsinghua University, Beijing 100084, China.

E-mail addresses: xiaoyu_liang@tsinghua.edu.cn (X. Liang), linfeng@tsinghua.edu.cn (F. Lin).

¹ These authors contributed equally to this work.

including multi-laser cooperation, beam shaping, ultrasonic assistance, and thermal field assistance. However, further in-depth research is required to fully understand these effects. One of the current major challenges in L-PBF process development is controlling the microstructural state of the material during formation, and consequently, tailoring the material's mechanical properties [8]. Stainless steels such as 316L that are highly workable and recyclable serve as the workhorse materials of our society. As industries such as aerospace, automotive, biomedical, and energy increasingly demand materials with exceptional mechanical properties, the need for advanced processes presents a challenge in meeting these requirements [9]. The characteristic rapid solidification in L-PBF brings about refined grain features combined with dendritic and cellular structures, as well as a high dislocation density. Wang et al. [10] reported 316L austenitic stainless steels fabricated by L-PBF a high tensile strength of 700 MPa while maintaining 50 % elongation. However, in engineering applications, the ductility of these single-phase FCC alloys is often excessive.

Strengthening methods for meeting the performance requirements of industrial applications typically involve methods such as plastic deformation (e.g., cold rolling, forging) and the construction of engineered gradient microstructures with spatial variations [11,12]. Yan et al. [13] achieved a remarkable enhancement in the strength of 316L stainless steel (SS) by employing a dynamic plastic deformation (DPD) process. Through this approach, a bulk nanostructured 316L SS composed of nanosized grains embedded with bundles of nanometer-thick deformation twins was synthesized, reaching a tensile strength of approximately 1.4 GPa. Lei et al. [14] pre-formed a gradient nanostructured (GNS) surface layer on 316L SS via surface mechanical rolling treatment (SMRT). Following subsequent annealing at 700 °C, the sample exhibited enhanced strength–ductility synergy. Despite the remarkable improvements in material properties achieved through various post-processing techniques, a major challenge remains: these methods inherently limit their applicability to geometrically complex, high-performance components [15].

Notably, the strength of 316L SS formed by the L-PBF process still lags behind that of the heterogeneous structured 316L SS achieved through post-treatment, while the additive-manufactured austenitic stainless steels, as non-heat-treatable materials that the strength can hardly be improved much by optimizing the process parameters [16]. The limitation in strength observed in austenitic stainless steel is attributed to the small laser-melted regions and the exceptionally high thermal gradients. StJohn et al. [17] reported that grain refinement is the result of the interdependence between nucleation and growth acting in concert within an environment dictated by the alloy chemistry. These factors significantly restrict the range of the supercooled zone [18], making it difficult to achieve a microstructure characterized by ultra-fine grains. Considering that the traditional alloy compositions are not designed for additive manufacturing processes, we also cannot expect materials with original alloy compositions to consistently exhibit superior performance in additive manufacturing. Han et al. [19] and Tan et al. [20] indicated that the addition of elements such as Ti and Nb promotes the activation of heterogeneous nucleation and enhances undercooling, which is expected to refine the grain structure and induce the formation of secondary phases. Our recent studies have demonstrated that the metallurgical characterization of L-PBF can lead to the in-situ formation of oxide particles and Nb- and Cr-rich precipitates in austenitic stainless steels, thereby strengthening the tensile performance [21].

By optimizing the additive manufacturing process of 316L SS to control grain size, composition, and phase distribution, the introduction of the hetero-deformation induced (HDI) strengthening mechanism not only preserves the ability to fabricate complex structures but also enhances the material's performance. This strategy holds great promise for expanding the application of 316L SS in high-end equipment manufacturing, aerospace, and energy sectors. Beyond the challenges of microstructural control during fabrication, one of the major obstacles in

additive manufacturing is the excessive cost of metal powders remains a substantial barrier. Additive manufacturing constructs parts layer by layer within a powder bed, with each new layer supported by both the underlying powder and the build platform. However, Alamos et al. [22] and Lutter-Günther et al. [23] reported that over 90 % of the total metal powder is unused during the process, significantly impacting the economic viability of this technology.

Based on the fundamental principles of advanced materials manufacturing, we innovatively propose the concept of liquid-metal-assisted laser powder bed fusion (LMA-L-PBF, Fig. 1), using liquid Sn with a low melting point and high thermal conductivity as the thermal management medium in the additive manufacturing process. This layer-by-layer *in situ* heat treatment further develops the rapid interlayer cooling characteristics of additive manufacturing, effectively addressing diverse strengthening challenges faced in the manufacturing process. On the other hand, the formation of the liquid-floating powder bed significantly reduces powder consumption during the fabrication process.

In this study, a heterogeneous microstructure is realized in austenitic steel, with grain refinement and grain boundary hardening as key mechanisms for enhancing strength. Here, we established a normalized process diagram by dimensionless process parameters, successfully controlling fine-grain regions. We analyzed the microstructure of the fine-grain regions using transmission electron microscopy (TEM), where dislocation cell walls are modified by abundant Nb and Cr nanoprecipitates, and a large number of oxygen-containing spherical particles are present in the FCC matrix. The deformation mechanism of this heterogeneous structural steel was studied through *in-situ/ex-situ* electron backscatter diffraction (EBSD), revealing that the dynamic formation of low-angle grain boundaries is closely related to high kernel average misorientation values. Additionally, the <001> preferred orientation in the fine-grained region is lower than that in the coarse-grained region. The synergistic effect of grain refinement and precipitation strengthening provides ultrahigh strength to the material while maintaining a high elongation. At last, the formation mechanism of the liquid-floating powder bed and the more cost-effective LMA-L-PBF manufacturing process are discussed in detail.

2. Elaboration on the liquid-metal-assisted laser powder bed fusion technique (LMA-L-PBF)

2.1. Equipment and processes

A self-developed LMA-L-PBF system (Fig. 1) was employed for sample fabrication, featuring a 500 W IPG fiber laser with an approximate spot size of 80 μm. The LMA-L-PBF technique integrates liquid Sn into the build chamber, where its high surface tension ensures that dense materials, such as 316L SS, remain consistently positioned above the liquid interface throughout the printing process. This innovative methodology significantly reduces the quantity of powder required and mitigates contamination risks to both the powder and the printed components during fabrication [24]. Furthermore, the advantageous properties of liquid Sn—including high thermal conductivity, a low melting point, and non-wetting characteristics—contribute to minimizing contamination risks during the printing operation.

Before the experiment, the build chamber was purged with inert argon gas to reduce oxygen levels below 50 ppm. Subsequently, solidified Sn was heated to 573 K (300 °C) for 1 h before the commencement of the printing process. To ensure effective melting and fluidity of liquid Sn [25] in the argon atmosphere and to balance the trade-off between the thermal conductivity and heat preservation of the liquid Sn during the additive manufacturing process, the temperature of the liquid Sn was ultimately maintained at 573 K. The effects of liquid Sn with higher temperatures (673 K, 400 °C) on microstructure and mechanical properties were discussed in Section 4.3. During printing, the laser selectively melts each layer, followed by the deposition of a new powder layer, repeating this iterative procedure until completion. The

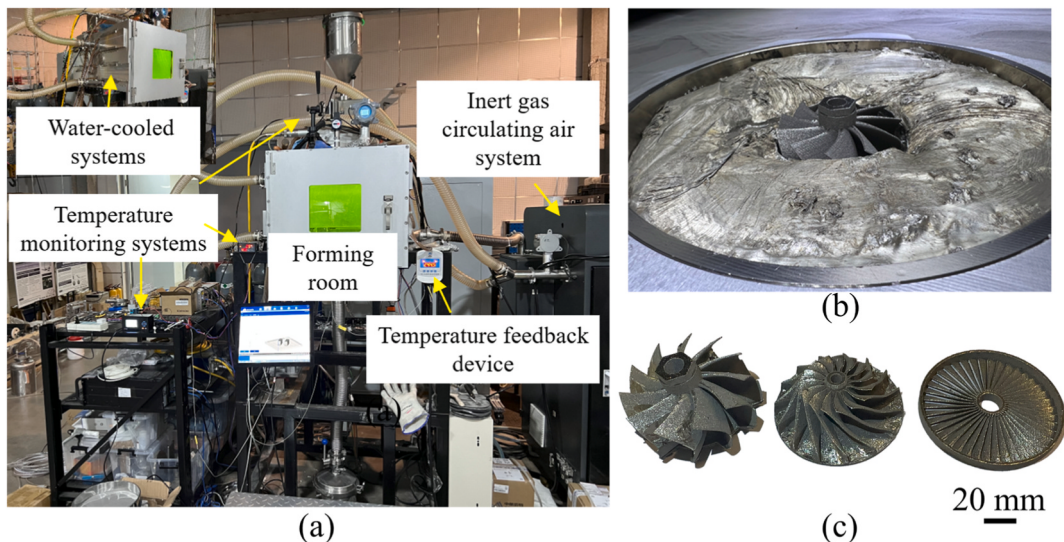


Fig. 1. (a) Schematic processing illustration of liquid-metal-assisted laser powder bed fusion. (b) A photo taken at the end of the LMA-L-PBF process: the part and the surrounding liquid metal are shown following the removal of the metal powder bed (c) Turbine rotors fabricated by LMA-L-PBF with three blade thicknesses (From left to right the thickest part of the blade decreases from about 2 mm to less than 1 mm).

fabrication of samples for mechanical property and microstructural analysis took approximately 12 h. After printing, the component was cooled to room temperature while submerged in liquid Sn, a process that lasted about 2 h. The Sn was then reheated to its melting point, facilitating the removal of the part, which required an additional 1 h.

2.2. Features of the liquid-metal-assisted laser powder bed fusion

The LMA-L-PBF process technology has three main features, as presented in Fig. 2(a–c). The most obvious feature comes from the thin layer of powder that always floats above the liquid metal during the powder spreading process, corresponding to a “liquid-floating powder bed” (Fig. 2(b)). In terms of density, stainless steel is greater than liquid Sn, but stainless steel powders (including others such as high-temperature alloy powders, titanium alloy powders, etc.) can float on liquid metal. In fluid mechanics, Bond Number (Bo) is an important dimensionless number used to describe the relative strength of the effects of gravity and surface tension.

$$Bo = \left(\frac{L}{\lambda_c} \right)^2 \quad \text{Eq. 1}$$

L denotes the Characteristic length (e.g., droplet diameter, pipe radius) and λ_c denotes the capillary length.

$$\lambda_c = \sqrt{\frac{\gamma}{\rho g}} \quad \text{Eq. 2}$$

In Eq. (2), γ represents the surface tension, ρ represents the density and g represents the acceleration of gravity. In the system of one LPBF metal powder acting with liquid Sn, assuming that the average powder particle size is 30 μm , the liquid Sn has a γ of 500 mN/m and g 7000 kg/m³ [26], the resulting bond number is 10^{-4} . Consequently, for a single metal powder, the surface tension provides a support effect that is approximately 10000 times the effect of gravity. Rather than one single powder, the floated powder layer is constituted of a plurality of metal particles that have been gathered and stacked. The requirement for balance of vertical forces, incorporating the weight of the sphere in addition to forces derived from surface tension and buoyancy, signifies that the line of contact (where the surface tension force is exerted) engenders an inclination. This tendency engenders a net horizontal force, thereby causing the spheres to clump together, rather than separate, making it

difficult for the liquid Sn to penetrate between the powder particles. As demonstrated in the Supplementary Video 1, there is no liquid Sn inside the powder layer; only the bottom powder particles are in contact with the liquid Sn, providing a surface tension that far exceeds their own weight. Equilibrium is attained through balancing the weight of the powders and the surface tension, resulting in the formation of a floating powder bed on the liquid Sn.

The second feature of the LMA-L-PBF is that the formed parts are fully immersed in liquid Sn rather than being encapsulated by the passive, layer-by-layer accumulation of powder. As can be seen in Fig. 2(a), the platform is plunger-type rather than piston-type and is designed to control the movement of the forming substrate. The liquid level remains horizontally stable even when the moving platform is raised and lowered. A thin layer of powder is always present on the forming plane, and the forming cylinder is kept almost completely filled with liquid Sn. This reduces the total amount of powder needed to print the part, as only enough powder is required to maintain the thin layer in the uppermost part of the forming cylinder. In contrast, with conventional powder bed fusion, the powder must fill the entire forming cylinder at the end of the print process. Furthermore, since liquid Sn cannot wet materials such as stainless steel or titanium alloys, after cooling the liquid Sn and the thin layer of powder separate automatically, as shown in Fig. 2(b). The powder can then be easily removed with a vacuum cleaner. Thus, the liquid Sn can be recycled.

The unique feature, albeit unintuitive, is the change in the thermal characteristics of the melting and solidification of the material during the LMA-L-PBF process. As shown in Fig. 2(c), liquid Sn has a much higher thermal conductivity than powder, which allows for more significant heat exchange in the deposited materials. The ability of liquid Sn to control the temperature of the forming environment at elevated temperatures enables LMA-L-PBF to conduct heat treatment concurrently. Furthermore, this synchronized heat treatment process does not alter the fast solidification characteristics of LMA-L-PBF, a feature of L-PBF technology. Heat transfer depends on the temperature difference, thermal conductivity and geometry. Although the LMA-L-PBF process involves a higher substrate temperature, which reduces the temperature difference between the melt pool and the forming environment, the higher thermal conductivity and larger contact area between the liquid Sn and the deposited material allow for potentially higher heat exchange. In this work, LMA-L-PBF can achieve an even faster solidification rate, as demonstrated in the Supplementary Materials through

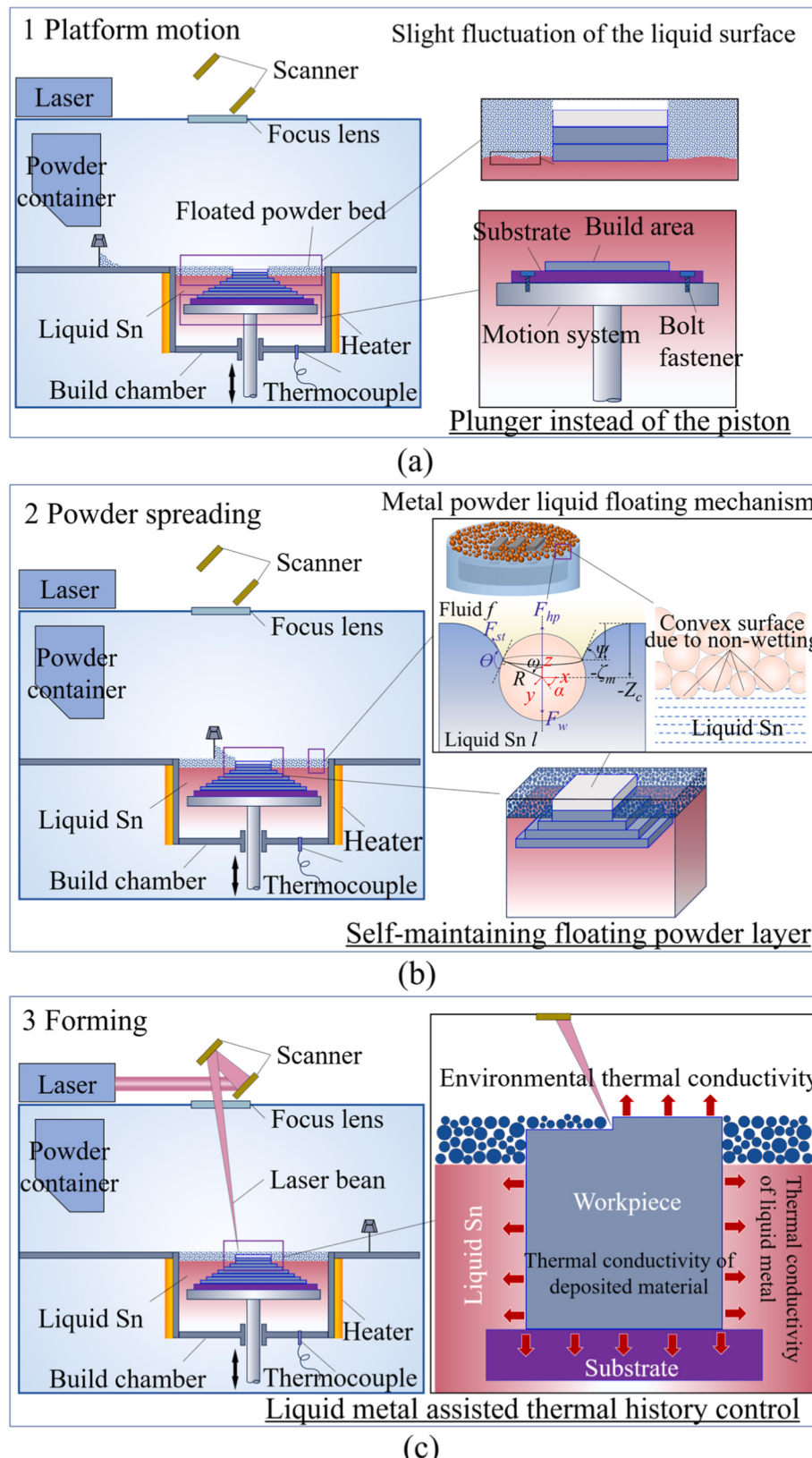


Fig. 2. The schematic diagram of the forming process is enclosed within the red dashed box, as shown in (a–c). During the LMA-L-PBF forming process, (a) the build platform descends layer by layer as the part height increases, (b) a powder spreading spreads a new layer of powder over the surface, and (c) a laser selectively fuses designated regions. This cycle repeats until the part is fully built. A foundational requirement for successful fabrication is that the movement of both the platform and the powder spreading must not disturb the integrity and flatness of the liquid-floating powder bed (a). Furthermore, the superior surface tension of the liquid metal stably supports the powder bed on its surface, enabling a cost-efficient manufacturing route (b). Notably, the excellent thermal conductivity of the liquid metal offers greater control over the evolution of the microstructure during solidification (c), providing opportunities to tailor material properties. (For interpretation of the references to colour in this figure legend, the reader is referred to the Web version of this article.)

simulation analyses. This rapid solidification process, combined with temperature-controlled, in-situ heat treatment, provides LMA-L-PBF with unique flexibility in microstructure control.

3. Materials and methods

3.1. Austenitic stainless steel powders

Atomized micro-alloyed 316L SS (hereafter termed MA-ASS) and standard 316L SS powders were synthesized through gas atomization in a high-purity argon atmosphere, resulting in particle sizes ranging from 15 to 53 μm (China Institute of Metals and Metallurgy, China), specifically tailored for the additive manufacturing process. The chemical compositions of both the powders and the resultant samples were analyzed using inductively coupled plasma optical emission spectrometry (ICP-OES). Detailed chemical compositions of the samples are presented in Table 1. In the supplementary materials, we provide a detailed explanation confirming that under the conditions of this study, Sn elements did not cause contamination of the materials. Aside from the non-wetting conditions between liquid tin and the metal, the low solubility of Fe near the melting point of Sn and the insufficient formation time prevented any reaction between Sn and the material. Furthermore, subsequent transmission electron microscope energy dispersive spectroscopy (TEM-EDS) analyses revealed that Sn did not dissolve into the matrix or exist in the form of intermetallic compounds. In Table 1, we attribute the trace presence of Sn to the measurement accuracy of the ICP technique. It is important to further clarify the rationale behind the choice of powder composition. The addition of Nb reduces grain boundary energy and influences solute atom segregation, while the incorporation of Ti promotes heterogeneous nucleation and inhibits further epitaxial grain growth. The concept of microalloying 316L powder with Nb and Ti to produce MA-ASS powder is inspired by the unique characteristics of the LMA-L-PBF process, namely, rapid cooling during fabrication. Specifically, this approach seeks to leverage the changes in undercooling induced by microalloying elements to maximize the ability of liquid metal-assisted additive manufacturing to tailor the microstructure.

3.2. Fully dense sample preparation

To obtain nearly fully dense samples, a series of control experiments were conducted by fabricating samples with dimensions of 30 mm (length) \times 10 mm (width) \times 10 mm (height). The processing parameters used in these experiments are presented in Table 2. We applied the normalized equivalent energy density method to identify an effective processing window for LMA-L-PBF, thereby elucidating the relationship between the 3D printing processing parameters and the porosity of the sample shown in Fig. 3. In this diagram, the dimensionless processing variables E_{min}^* and $1/h^*$ are represented on the x- and y-axes, respectively. Here, E_{min}^* and h^* were defined as:

$$E_{min}^* = \frac{p^*}{v^* l^*} = \frac{Ap}{2\nu lr_b \rho C_p(T_m - T_0)} \quad \text{Eq. 3}$$

$$h^* = \frac{h}{r_b} \quad \text{Eq. 4}$$

Table 1

Chemical compositions of the MA-ASS and 316L SS powder and samples (wt.%).

| | Fe | Cr | Mo | Mn | Ni | Si | C | Nb | Ti | Sn |
|----------------|------|-------|------|------|-------|------|------|------|------|-------|
| MA-ASS powder | Bal. | 18.17 | 2.06 | 0.12 | 10.66 | 0.23 | 0.03 | 0.56 | 0.03 | <0.01 |
| MA-ASS sample | Bal. | 17.49 | 2.16 | 0.32 | 11.46 | 0.35 | 0.02 | 0.45 | 0.01 | <0.01 |
| 316L SS powder | Bal. | 17.85 | 2.00 | 0.21 | 12.20 | 0.25 | 0.03 | – | – | <0.01 |
| 316L SS sample | Bal. | 17.84 | 2.16 | 0.49 | 10.82 | 0.34 | 0.01 | – | – | <0.01 |

Table 2

Processing parameters of additive manufacturing.

| Manufacturing parameters | Value | |
|---------------------------|---|---------|
| Laser hatching parameters | Laser power (W) | 175–300 |
| | Laser scanning velocity (v , mm/s) | 600–800 |
| | Layer thickness (t , μm) | 30 |
| | Hatch distance (h , μm) | 100 |
| | Hatch angle (θ , °) | 67 |
| Laser contour parameters | Laser power (W) | 125 |
| | Laser scanning velocity (v , mm/s) | 1000 |
| Liquid Sn temperature | 573 K (300 °C) | |

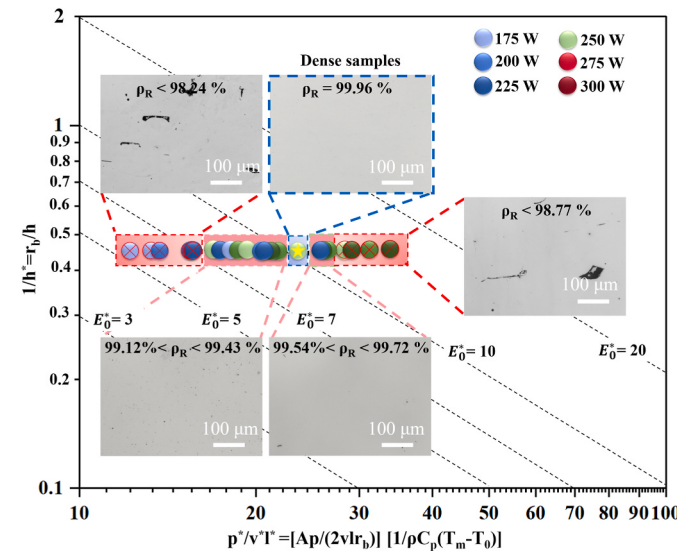


Fig. 3. The normalized processing diagram for MA-ASS produced via LMA-L-PBF is presented, featuring isopleths of normalized equivalent energy density (E_0^*) that define regions of energy-efficient processing, as indicated by dashed lines. The optimized processing parameters utilized in this study are highlighted within the blue and red regions. Processing conditions that resulted in samples with relative densities (ρ_R) exceeding 99.9 % are enclosed within blue dotted boxes, while those yielding relative densities below 99.9 % are enclosed within red dotted boxes. Insets present representative optical micrographs of cross-sectional views. (For interpretation of the references to colour in this figure legend, the reader is referred to the Web version of this article.)

Where E_{min}^* represents the normalized minimum Volumetric Energy Density (VED) required to melt a material; the variables p^* , v^* , l^* and h^* denote the dimensionless laser power, scan speed, layer thickness, and hatch spacing, respectively. The parameters are defined as follows: A is the surface absorptivity (~0.35), p the laser power, v the scan speed, l the layer thickness, h the hatch spacing, r_b the laser beam radius (4×10^{-5} m), ρ the density of 316L SS powder (4210 kg/m³), C_p the specific heat capacity (~502 J/kg/K, estimated by using the weight averaging method), T_m the melting temperature of 316L SS (1673 K, measured by differential thermal analysis), and T_0 the powder bed temperature. The details of the calculations are discussed in Refs. [10,27,28]. By employing the normalized equivalent energy density method, we established an effective laser processing window for the fabrication of

fully dense 316L SS samples. The E_0^* serves as a convenient tool for delineating the complex relationship between processing parameters. By adjusting the additive manufacturing process parameters to optimize E_0^* , successfully producing near fully dense ($>99.9\%$) samples within the energy density range of $7 \leq E_0^* \leq 14$. In contrast, energy densities in the range of while $0 < E_0^* < 7$ result in lack-of-fusion defects, while values of $E_0^* > 14$ lead to the onset of keyholing.

3.3. Microstructure characterizations

The specimens were mounted on a Struers CitoPress inlay machine and mechanically polished using silicon carbide paper, achieving a 2000-grit finish. Microstructural analysis was conducted utilizing a field emission scanning electron microscope (FESEM, Zeiss Sigma 360), equipped with a backscatter electron (BSE) detector. For precise characterization of microstructural features, including grain morphology, size, and orientation, electron backscattered diffraction (EBSD) was applied, with a scanning step size of 0.65 μm . The microstructural evolution of the samples, both prior to and following tensile deformation, was investigated using a FEI Tecnai G2 F20 transmission electron microscope (TEM). Selected area electron diffraction (SAED) and energy dispersive spectroscopy (EDS) were employed to examine the microstructural characteristics and ascertain the chemical compositions of the samples. For TEM samples preparation, SEM with a focused ion beam (FEI Scios) was used to prepare site-specific TEM foils. High-angle annular dark-field (HAADF) scanning transmission electron microscopy (STEM) imaging was performed using an aberration-corrected FEI Titan Themis microscope. The acceleration voltage was set to 300 kV. The distribution of inclusions was quantified by analyzing backscattered SEM images from at least six distinct locations per specimen, utilizing

ImageJ image processing software (National Institutes of Health, USA), in accordance with ASTM E1245 standards [29].

3.4. Uniaxial tensile

For tensile testing, dogbone-shaped specimens were fabricated from the as-built components using electrical discharge machining, with gauge dimensions of 10 mm in length, 3.0 mm in width, and 1.5 mm in thickness. Prior to testing, the samples were polished to a final surface finish of 2000 grit using silicon carbide paper, in accordance with standard mechanical polishing protocols. The specimens were then cleaned with distilled water and acetone to remove any contaminants. Room temperature tensile tests were conducted using a Material Testing System (MTS) tensile testing machine equipped with a digital image correlation system at a strain rate of 0.1 % s^{-1} . To ensure reproducibility, a minimum of three tensile samples were tested, and the average values were reported. The yield strength was determined using the 0.2 % offset plastic strain method. Additionally, at a certain unloading strain, the specimen was unloaded in a load-control mode at an unloading rate of 10^{-3} s^{-1} , followed by reloading to the same applied load. The evolution of back stress and effective stress was analyzed from the unloading branches at various strains, employing an offset plastic strain of 0.01 % and a slope corresponding to Young's modulus (E), consistent with the Dickson method [30].

4. Results

4.1. Microstructural evolution

To qualitatively compare the effects of various processing parameters on microstructures, we constructed a normalized processing

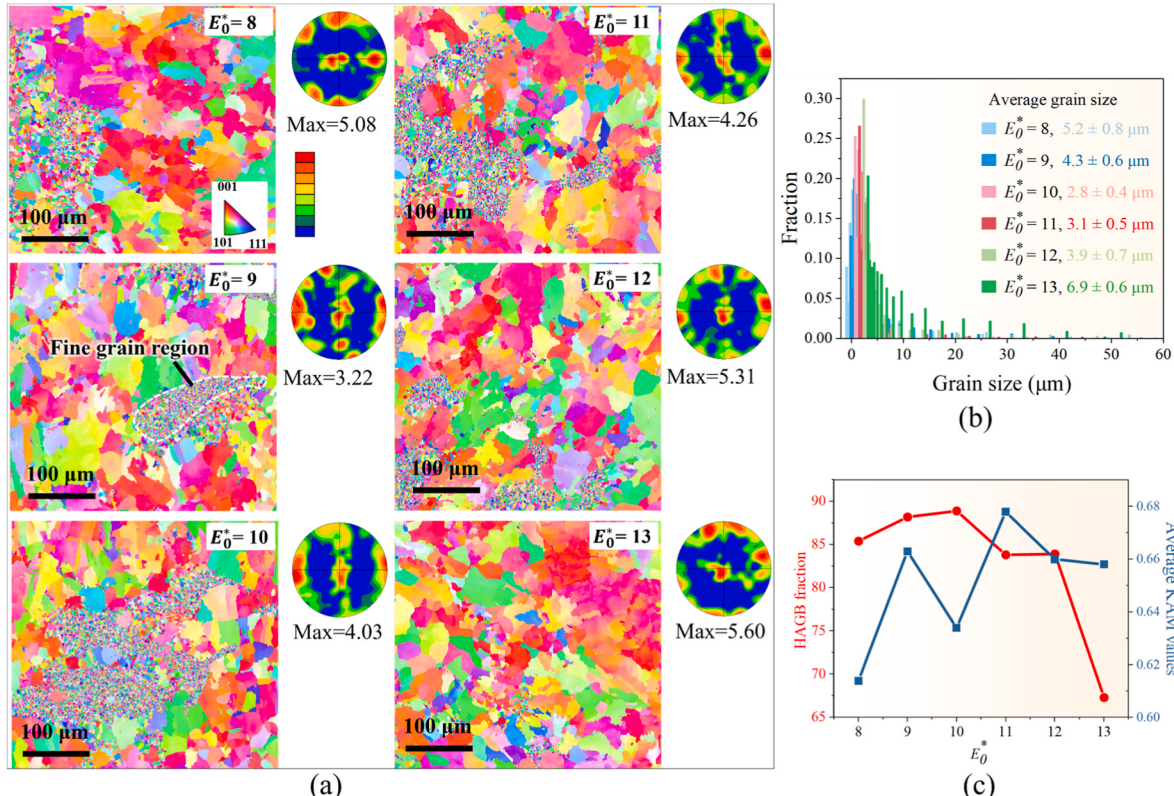


Fig. 4. (a) Horizontal cross-sectional EBSD images show the ability of LMA-L-PBF to tune the heterogeneous structure at different values of the normalized equivalent energy density. The value of E_0^* will influence the size of the fine-grain region since insufficient thermal input activates the heterogeneous nucleation of the material, while excessive thermal input will result in grain growth. (b) Average grain size results in different E_0^* values. (c) Changes in HAGB's fraction and average KAM values as a function of E_0^* .

diagram for the LMA-L-PBF process, as shown in Fig. 3. By adjusting the laser heat input, we were able to influence the activation of heterogeneous nucleation of MA-ASS at the solid-liquid interface, demonstrating the capability to control the microstructure in LMA-L-PBF (Fig. 4). Within the dense forming region, as the energy density increases, the samples exhibit fine-grain regions of varying sizes (Fig. 4(a)), accompanied by changes in texture orientation. The texture intensity exhibits an initial decrease followed by an increase. In the fine-grained regions, reduced grain size restricts crystal growth directions, leading to a more random grain orientation and thus hindering the development of a pronounced texture. We further characterized the grain morphology, size, and orientation on planes perpendicular and parallel to the building direction of these samples, as shown in Supplementary Fig. 1. The grain size distribution and the variation in average grain size, as depicted in Fig. 4(b), reveal that with increasing input energy, the area of fine-grain regions increases and then decreases. This variation can be attributed to the differing thermal management mechanisms induced by liquid Sn under varying laser parameters. In Fig. 4(c), a lower kernel average misorientation (KAM) value is associated with a higher proportion of high-angle grain boundaries (HAGBs). Specifically, the high preheating of liquid tin promotes forming at lower laser heat inputs, whereas higher laser heat inputs lead to increased heat dissipation. This phenomenon can be further interpreted as the realization of substrate preheating in each layer of the powder bed during the forming process.

According to the Hall-Petch relationship [31], grain size is directly related to material strength, meaning that smaller grain sizes lead to higher yield strength and can also enhance material ductility. Moreover, texture strength and the area/average grain size of the fine-grain regions are correlated, showing a trend of initially decreasing and then increasing. This behavior is understandable given the layer-by-layer melting and solidification characteristic of additive manufacturing, which promotes the formation of preferential $<001>$ texture orientations within the material. However, as a large number of equiaxed grains are formed, the competition and coexistence of various orientations result in a relatively random direction of grain growth.

Further, we employ combinations of laser parameters that fall near the $E_0^* \sim 10$ isopleth line. Equiaxed fine grains and fine-grain regions were observed in the horizontal sections of MA-ASS fabricated by LMA-L-PBF. The microstructure exhibited a heterogeneous microstructure in different building orientations, as shown in Fig. 5(a), with interspersed equiaxed grain regions and clustered fine-grain regions. Of particular interest is the refined average grain diameter of $2.05 \mu\text{m}$ – $3.72 \mu\text{m}$ of MA-ASS (Fig. 5(b)). It should be noted that the larger the fine-grain region, the smaller the multiple of uniform distribution (MUD) value of the pole figure (PF), indicating that the preferential growth direction of the grains becomes more random. A comparison of the grain structure illustrated in Fig. 5(c) and (e) indicate that there is a direct correlation between low-angle grain boundaries (LAGBs, 2° – 15°) and orientation

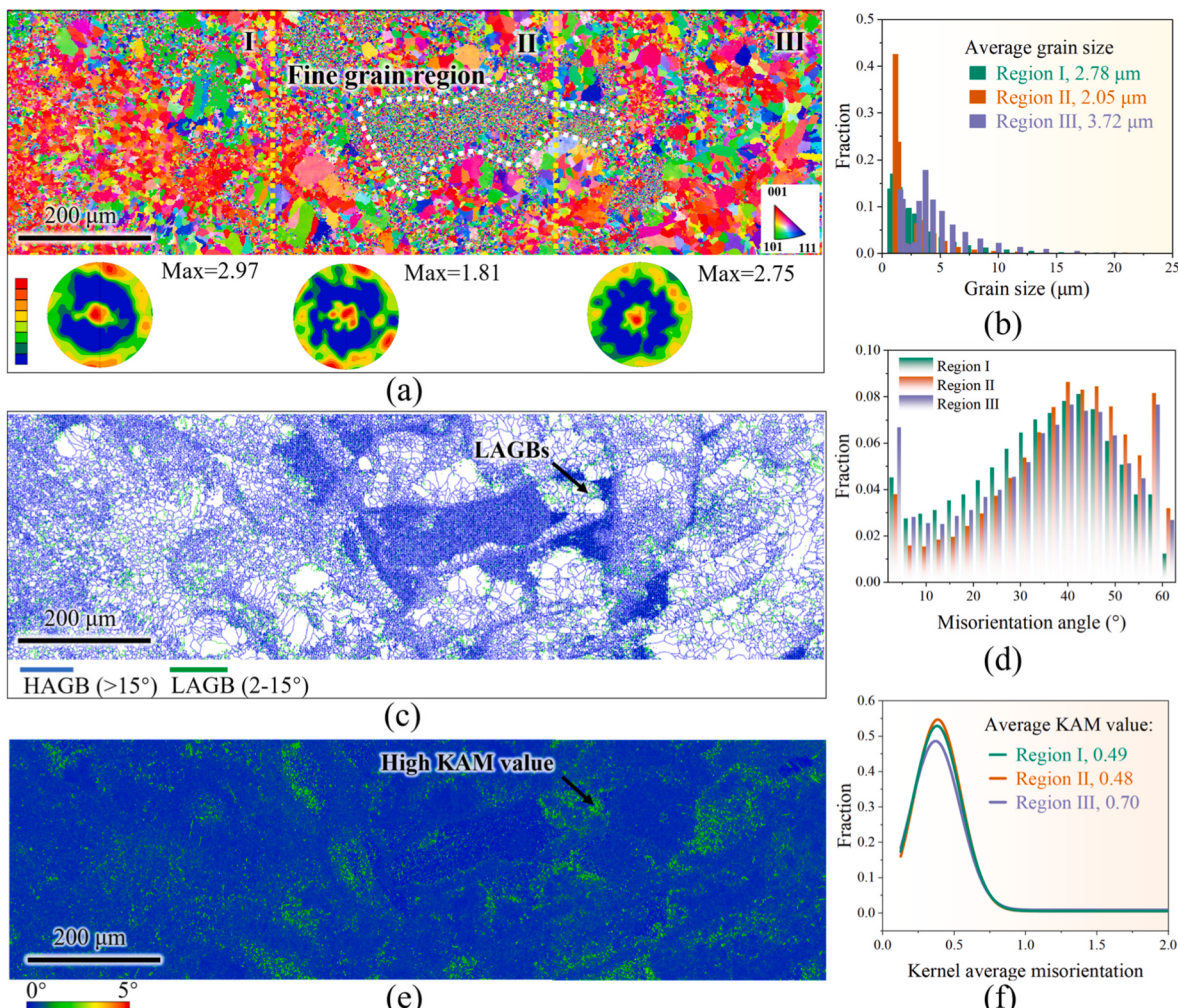


Fig. 5. EBSD images of the horizontal cross-section from the MA-ASS fabricated by LMA-L-PBF, showing: (a) the distribution of grain morphology at different scales and orientations; (b) the average grain size results; (c) boundaries defined by different misorientation angles; (d) the misorientation angle distribution results. The terms HAGBs and LAGBs refer to high-angle grain boundaries and low-angle grain boundaries, respectively. (e) The average misorientation angle between a point and its neighbors, which serves as an indicator of the dislocation density of geometrically necessary dislocations, and (f) the KAM angle distribution result.

deviation. The neighborhood of LAGBs has higher kernel average misorientation (KAM) values, as indicated by the black arrows. During the additive manufacturing process, the rapid cooling rate of liquid Sn facilitates grain boundary transition. The LAGBs with lower grain boundary energy [32] will continue to absorb dislocations as the internal stored energy increases. Fig. 5 (d) presents the distribution of misorientation angles across different regions. The fractions of high-angle grain boundaries in regions I, II, and III are 86.4 %, 91.3 %, and 85.4 %, respectively. Notably, the highest proportion of HAGBs $>15^\circ$ is observed in the fine-grained region. Fig. 5(f) illustrates the distribution trends of KAM values in these regions. The average KAM values vary among the regions, with region III, which possesses the largest average grain size, exhibiting the highest mean KAM value. Clearly, Fig. 5 (d) and (f) show that as the fine-grain region increases, or in other words, as the average grain size increases, the proportion of high-angle grain boundaries decreases (Regions I, II, and III are 86.4 %, 91.3 %, and 85.4 %, respectively). The higher KAM values are associated with lattice deformations and their distribution, indicating a high density of lattice defects and density of dislocations within the grains.

Fig. 6 illustrates the origins of the heterogeneous microstructure of MA-ASS fabricated by LMA-L-PBF. The schematic microstructure of MA-ASS fabricated by LMA-L-PBF is shown in Fig. 6(a). The matrix is punctuated by oxide nanoparticles, and the cell boundaries are reinforced by nanoprecipitation phases. The backscattered electron (BSE) mode of the electron microscope shows a large aggregation of spherical nanoparticles in the dendritic regions and their vicinity in the fine-grain region (Fig. 6(b)). To identify the specific composition of these nanoparticles, TEM characterization was performed on this region. The TEM-EDS results reveal that these aggregated particles are Ti-containing oxides (Supplementary Fig. 2). In contrast to the grain morphology observed in the horizontal section, Fig. 6(c) and (d) illustrate agglomerated equiaxed grains at the bottom of the melt pool and the formation

of large grains with high aspect ratios. More importantly, as revealed in Fig. 6(c), the equiaxed region is primarily concentrated at the bottom of the melt pool. This phenomenon can be attributed to that heat dissipation varies at different locations within the melt pool during the additive manufacturing process [33]. The higher cooling rate at the bottom leads to microstructural refinement, and rapid cooling of liquid Sn effectively promotes the formation of fine grains, enabling microstructural adjustment at the micron scale [34], which may correspond to the fine-grained zone in the top view shown in Fig. 5.

4.2. Fine-grain structures

Further microstructural characterization in the fine-grain region (Fig. 7) using TEM revealed that the boundaries of submicron-sized honeycomb cellular structures were modified by a combination of Cr- and Nb-rich nanoscale precipitates and dislocation cell walls (Fig. 7(a) and (g1-g10)). And corresponding energy-dispersive spectroscopy (EDS) images show that oxygen during the forming process reacts *in situ* with Mn, Si, and Ti to form 20 nm–100 nm nanoprecipitates (Fig. 7(e)). The high-resolution transmission electron microscopy (HRTEM) in Fig. 7(b) and (c) reveal the specific morphology of oxygen-containing nanoparticles, which are believed to be MnSiO_3 and TiO_2 [35]. These non-coherent oxide particles can pin dislocations during deformation, enhancing strength through the Orowan mechanism [36]. Fig. 7(d) and (e) show the rapid solidification cellular boundaries in the fine-grain region were decorated by a combination of dislocation walls and these nanoprecipitates, which are driven by the degree of undercooling (G/R ratio) and the surface tension of the solute-rich liquid [37]. The liquid metal acts as a heat exchanger during the early solidification of the melt pool; the increased degree of undercooling significantly enhances the nucleation rate [38]. The rapid solidification structure is reinforced by the presence of a typical

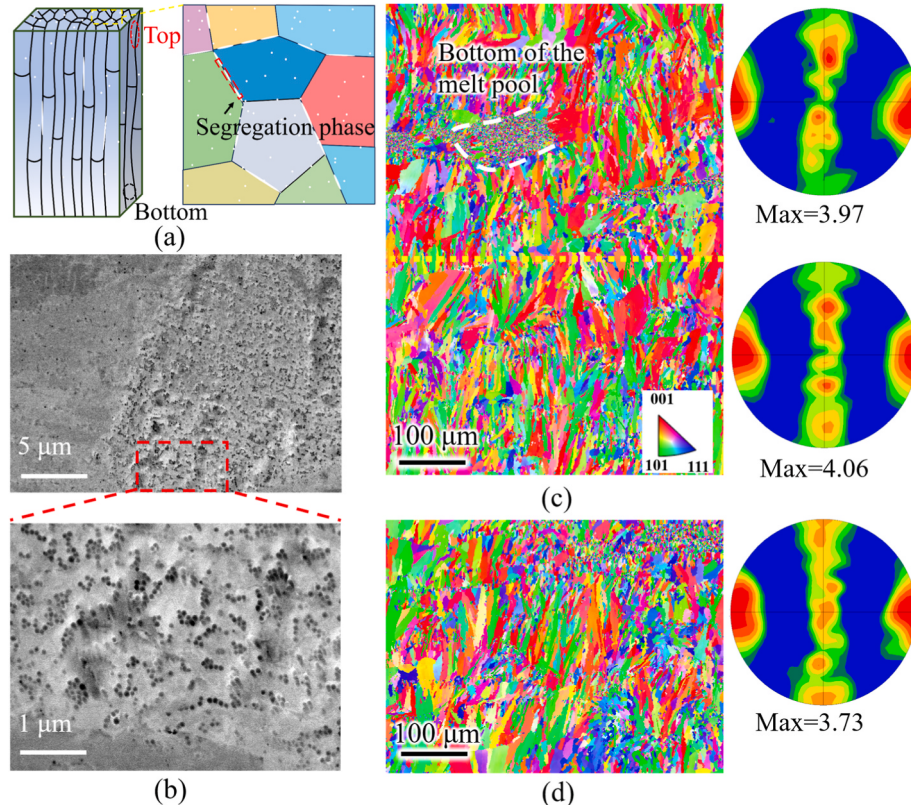


Fig. 6. (a) Schematic microstructure of MA-ASS fabricated by LMA-L-PBF. (b) Vertical cross-sectional BSE image reveals fusion boundaries and oxide nanoparticles, and the enlarged view shows some of them even clustered in groups. (c and d) Vertical cross-sectional EBSD images of the MA-ASS fabricated by LMA-L-PBF on the top (c) and bottom (d), respectively, which show the regions of fine-grain clusters at the edge of the melt pool (white dotted line).

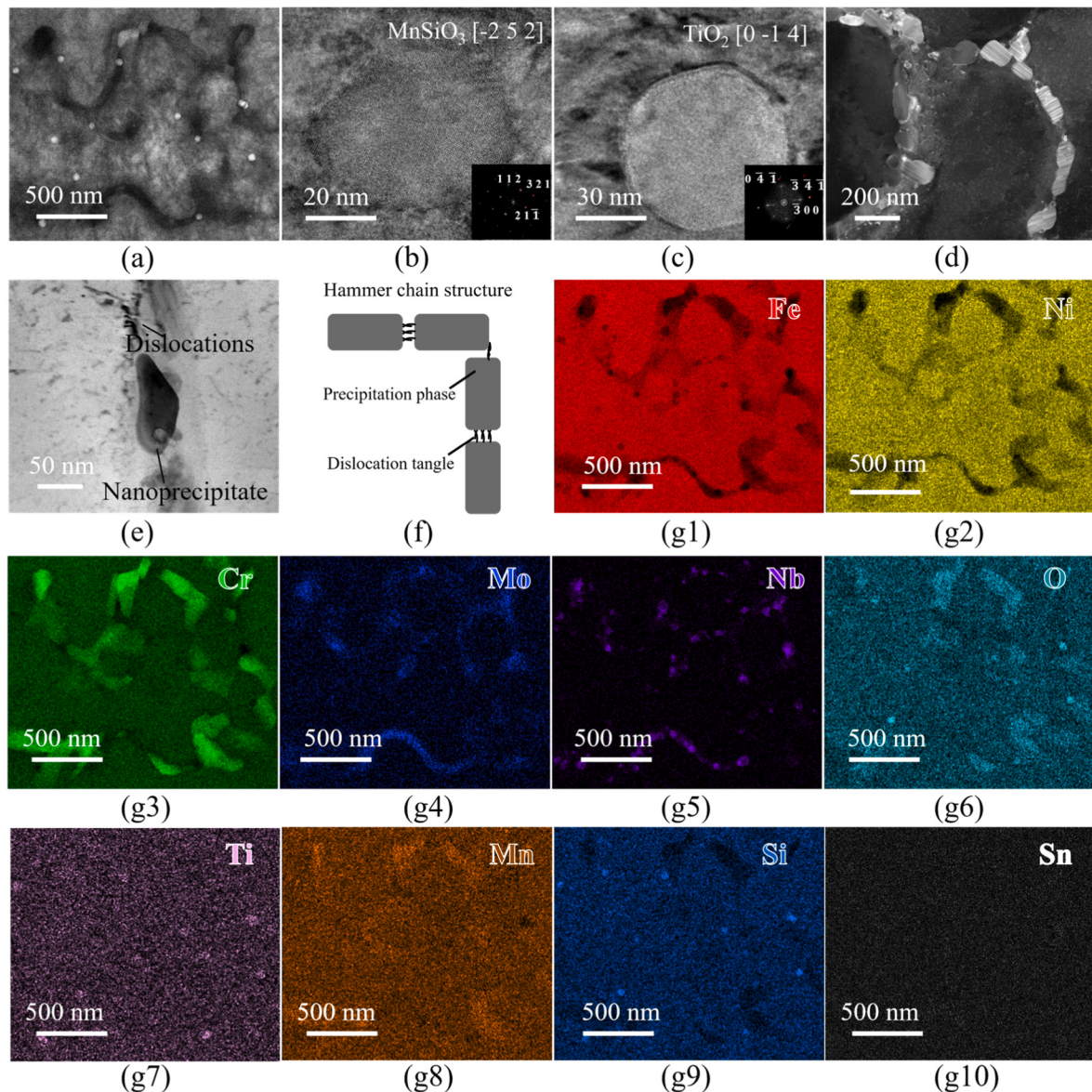


Fig. 7. (a) A bright-field TEM and (g1-g10) corresponding EDS images show the segregation of Cr, Mo, Nb, O, Ti, Mn, and Si elements to the solidification cellular walls. The HRTEM images of the nanoprecipitates, which are shown to be (b) MnSiO₃ and (c) TiO₂, respectively. (d) The dark-field TEM images showed that the cell boundaries of MA-ASS are modified by a high density of nanophases. (e) Enlarged view of the precipitates along the dislocation cell walls. (f) Schematic diagram of "hammer chain" structure.

"hammer chain" structure (Fig. 7(f)), replacing the traditional strengthening mechanism of storing high dislocation densities in 316L SS only.

The bright-field TEM and corresponding EDS images of nanophases in Fig. 8(a) exhibit the Cr-rich and Nb-rich nanoprecipitation phase along the solidification cell walls suppresses grain-boundary migration, thus favoring the formation of near-equiaxed grains. It is worth noting that Mo segregation near the cell boundaries typically contributes to the strengthening of the microstructure. The HRTEM further reveals significant structural differences between the nanoscale precipitates and the matrix (Fig. 8(b)). These Cr-rich precipitates, averaging approximately 110 nm in size, along with Nb-rich precipitates of around 30 nm, are incoherently embedded within the FCC matrix. This structural configuration effectively impedes the dissociation of dislocations in the FCC matrix during deformation. Furthermore, an aberration-corrected scanning transmission electron microscope high-angle annular dark field (STEM-HAADF) micrograph (Fig. 8(c)) reveals that the spacing of the observed vacancy arrays ranges from a few nanometers to several

tens of nanometers. Based on TEM-EDS characterization of the precipitate phase, these features are likely attributable to secondary phases or interfacial regions within the precipitates. To obtain high-resolution EDS maps for the respective elements and illustrate their density variations (Fig. 8(d)), thin and clean samples were used, with extended dwell times and low beam currents to achieve an optimal signal-to-noise ratio. The corresponding EDS maps, along with the element composition percentages, are shown in the inset (Fig. 8(d)). Fig. 8(e) reveals that Cr and Fe exhibit a more similar degree of homogeneity compared to Ni. Line scans of atomic fractions extracted from the EDS maps, as shown in the inset of Fig. 8(d), further support this observation, indicating that the atomic fractions of Cr, Fe, Mo, and Ni in each projection atomic column fluctuate randomly. The Ni atomic fraction shows minimal variation, while the atomic fraction of Cr exhibits the widest fluctuation range, occasionally exceeding a high point of 30 % or dropping below a low point of 22 %.

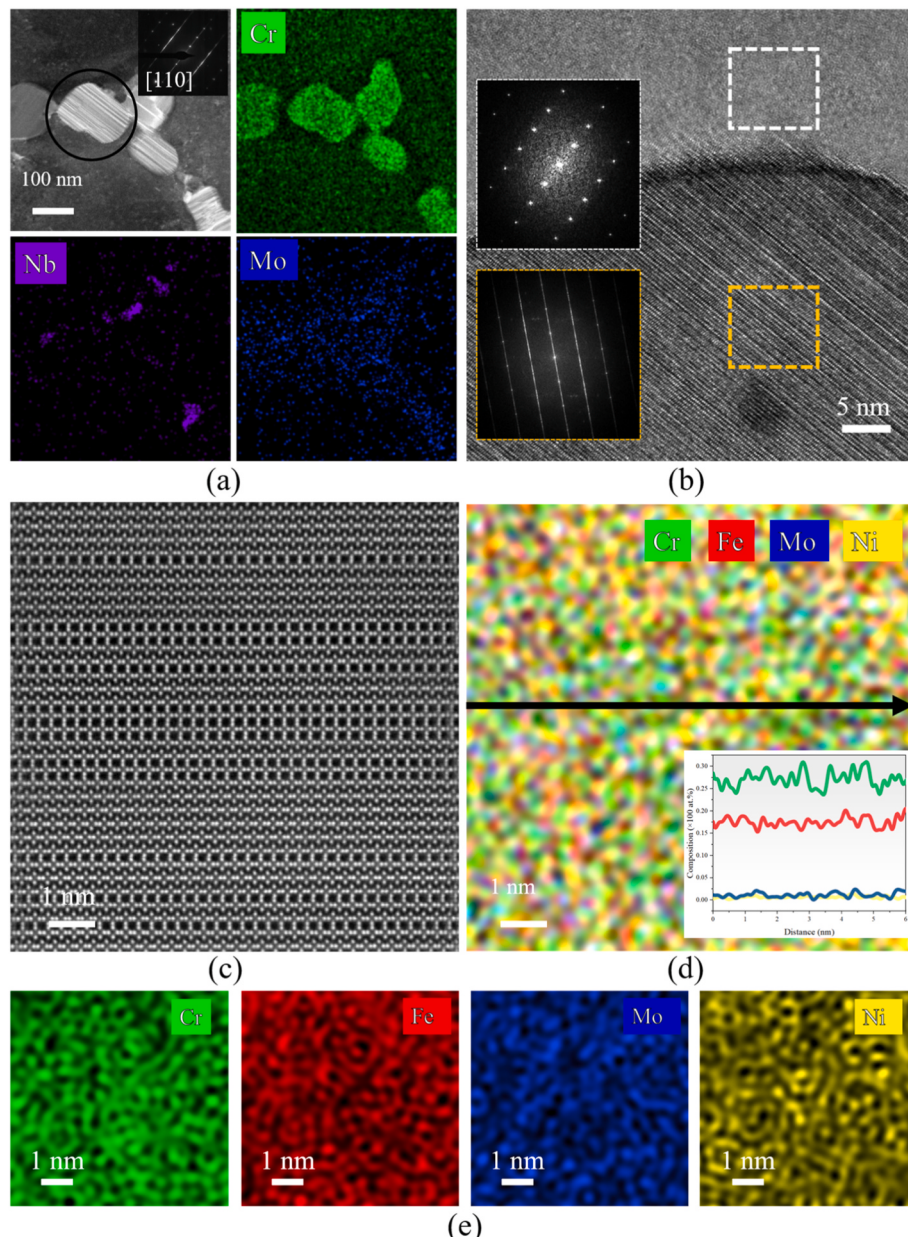


Fig. 8. (a) The bright-field TEM image of nanophases and its corresponding EDS maps. The SAED patterns is shown in the inset. (b) The matrix and precipitated phases show a non-congruent relationship under HRTEM. The FFT patterns inside the nanophases corresponding to the internal structure of the nanophase show significant differences from those of the matrix. (c) STEM-HAADF images for the [110] crystal axis with differently adjusted contrast to reveal secondary phases or interfacial regions inside the Cr-rich nanophase, and (d) corresponding EDS maps for Cr, Fe, and Mo. The inset presents line-scan EDS data, providing a one-dimensional compositional profile across selected atomic columns. (e) Magnification of local regions in (d) (all to the same scale), showing small groups of neighboring atomic columns with similar brightness.

4.3. Tensile properties

Both the engineering (Fig. 9(a)) and true (Fig. 9(b)) stress-strain curves from quasi-static uniaxial tensile tests reveal that the yield strength (σ_y , at 0.2 % offset) of 316L SS fabricated by LMA-L-PBF exceeds 600 MPa and 750 MPa, respectively. Notably, MA-ASS fabricated by LMA-L-PBF exceeds 1.1 GPa, while its ultimate tensile strength (σ_{UTS}) surpasses 1.5 GPa, significantly higher than that of the 316L SS. It is important to note the variability in the strengthening results for MA-ASS and 316L SS, with the very high strength originating from the intercellular precipitation of nanoprecipitation such as Nb-rich and Ti, while the key to the strength-ductility trade-off lies in the proper grain refinement and in-situ generation of oxides (the mechanism of the strengthening of 316L SS is covered in the 4.2). The tensile properties corresponding to

each data point from our study are presented in Table 3. Fig. 9(c) demonstrates that the strain hardening rate of MA-ASS exhibits multi-stage characteristics, with the LMA-L-PBF samples consistently displaying higher strain hardening rates than L-PBF samples prior to necking. This enhanced performance is attributed to the heterogeneous microstructure, which plays a pivotal role in generating substantial additional strain hardening [39]. As strain exceeds 3 %, the strain hardening rate of LMA-L-PBF gradually decreases from approximately 7 GPa to about 2 GPa before necking occurs, a behavior attributed to dislocation pinning.

To further highlight the exceptional strength-strain hardening synergy of LMA-L-PBF samples, we compared their uniform elongation and ultimate tensile strength to those of the L-PBF samples fabricated in this study (Fig. 9(d)). Additionally, their performance was compared with

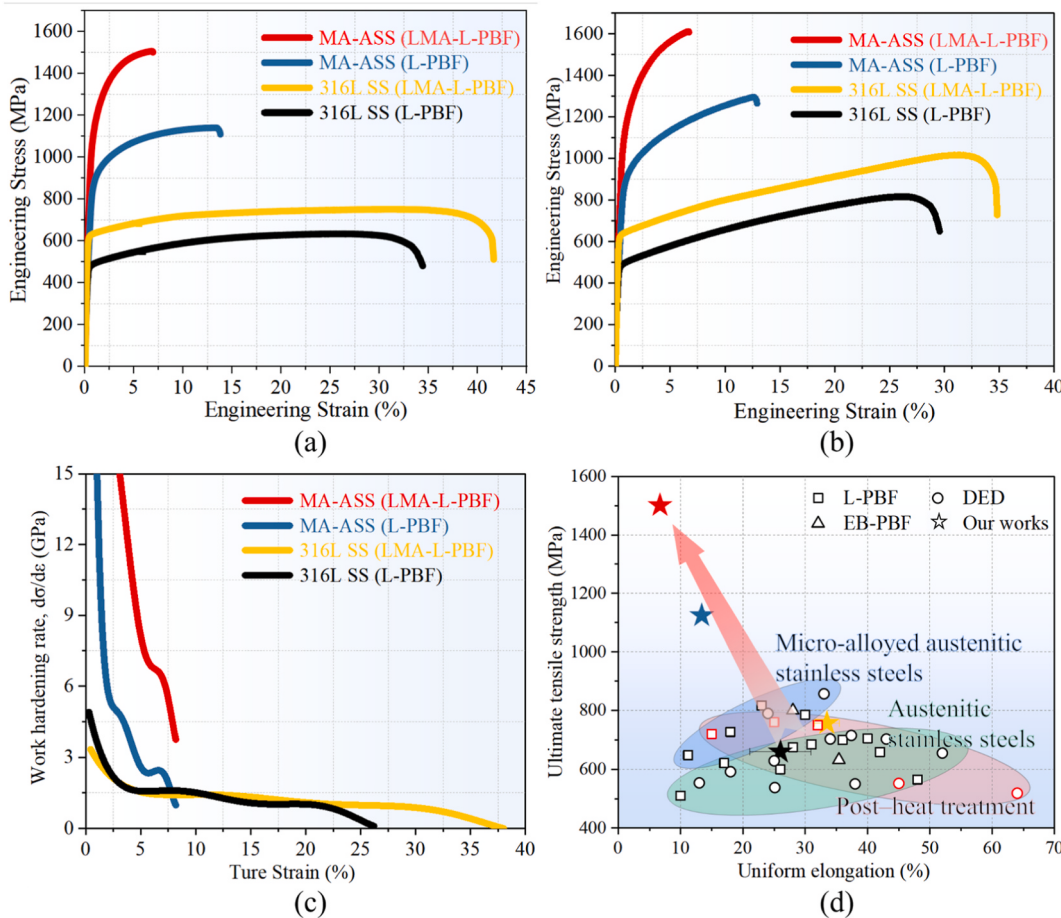


Fig. 9. Strain hardening and the strength-ductility combination of MA-ASS and 316L SS are presented as follows: (a) tensile engineering and (b) true stress-strain curves of samples fabricated by L-PBF and LMA-L-PBF, respectively; (c) the corresponding strain hardening rate and true strain relationships; and (d) a summary of ultimate tensile strength versus uniform elongation for additively manufactured 316L SS, including data from our work, laser powder bed fusion, directed energy deposition, and electron beam powder bed fusion. The exceptional combination of strength and ductility observed in 3D-printed steels (our work) surpasses that of high-performance 316L SS [57]. The tensile properties of each data point from our work are shown in Table 3.

Table 3
The mechanical properties of samples in optimized parameters.

| Process | Powder | σ_y (Mpa) | σ_{UTS} (Mpa) | Uniform elongation (%) | Elongation (%) |
|-----------|---------|-------------------|----------------------|------------------------|----------------|
| LMA-L-PBF | MA-ASS | 1138.9 ± 4.9 | 1501.1 ± 8.7 | 6.7 ± 0.4 | 6.9 ± 2.2 |
| | 316L SS | 613.0 ± 2.3 | 756.7 ± 10.5 | 33.5 ± 2.0 | 43.4 ± 4.3 |
| L-PBF | MA-ASS | 828.3 ± 17.32 | 1124.3 ± 16.6 | 13.4 ± 0.2 | 14.2 ± 0.6 |
| | 316L SS | 491.7 ± 18.5 | 659.6 ± 7.2 | 26.0 ± 4.9 | 34.9 ± 4.6 |

other additively manufactured 316L SS and MA-ASS produced via various methods, including laser powder bed fusion [35,40–45], direct energy deposition [19,46–50], and electron beam powder bed fusion [51–54]. The remarkable mechanical properties of LMA-L-PBF MA-ASS at room temperature are primarily attributed to the Hall-Petch effect and nanoprecipitation [38,49], where refined grains increase the grain boundary area per unit volume. Furthermore, the high density of nanoscale precipitates impedes dislocation motion and subcell movement, thereby activating the Orowan bypass mechanism [55]. While traditional strengthening mechanisms, such as the Orowan bypass, enhance the microstructure, they also impede dislocation motion, leading to a reduced accumulation of dislocations within the fine structure (e.g., diminished strain hardening). In contrast, during LMA-L-PBF processing, both dislocation formation and elemental segregation are modified. The transition from diffusion-mediated solidification to diffusion-limited solidification creates favorable conditions for the pre-existence of nanoscale dislocation units and precipitates

around submicron-sized solidification cells. These nanoscale features effectively impede the migration of newly formed dislocations, thereby enhancing the mechanical properties of the alloy. The synergistic effects of these strengthening mechanisms, combined with the grain size distribution [56], contribute to the unexpectedly high strength of MA-ASS.

4.4. The evolution of back stress and effective stress

The plastic deformation of multi-scale heterogeneous structures is inherently associated with complex stress-strain states, characterized by intricate distributions and interactions between distinct structural scales. In particular, during the early stages of plastic deformation, notable stress redistribution and back-stress effects are frequently observed [58]. Through a series of tensile loading-unloading-reloading experiments shown in Fig. 10(a) and (b), we quantified that the back-stress in LMA-L-PBF samples at approximately 1 % strain (corresponding to a 0.2 % offset) reached a remarkable 722.2 MPa (Fig. 10(c)),

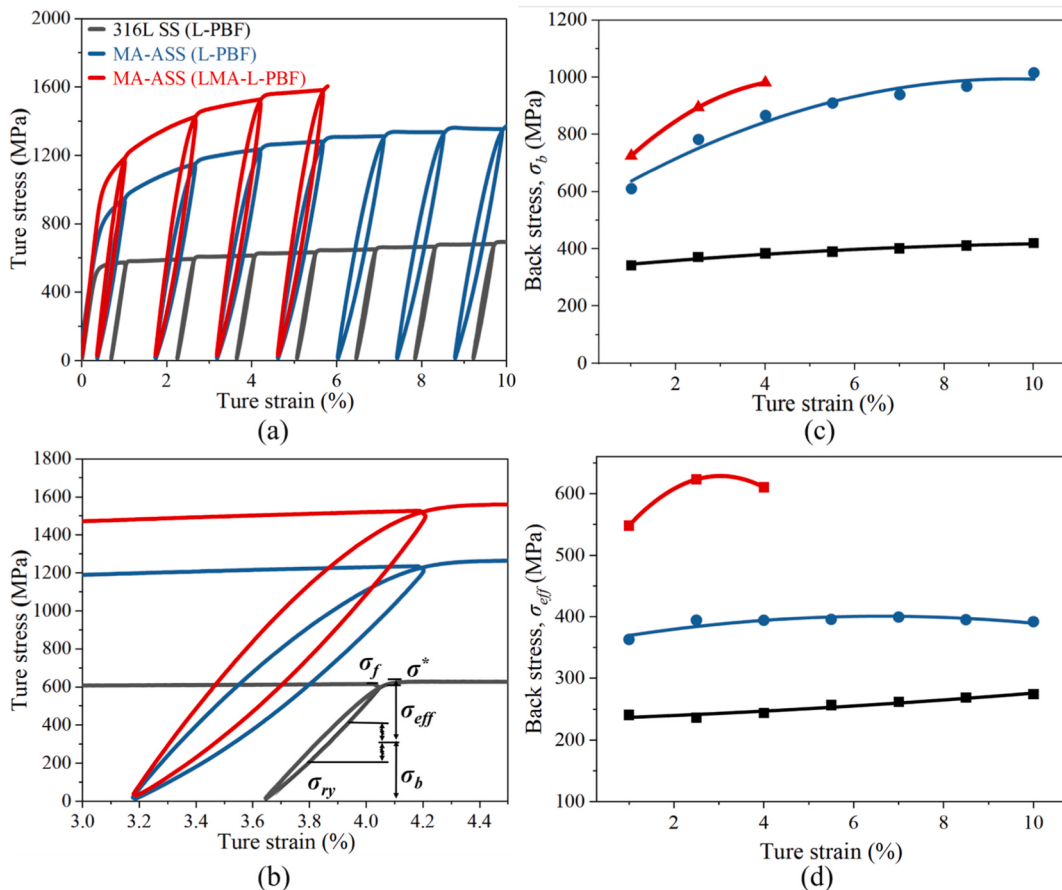


Fig. 10. (a) The true stress-strain curves obtained during loading and unloading for both MA-ASS and 316L SS samples are presented. (b) Back stress σ_b and effective stress σ_{eff} were calculated based on Dickson's method [59], using a magnified view of the unloading-reloading branch of these samples. Here, σ_{ry} refers to the reverse yield stress, and σ^* represents the stress range beyond the peak stress. (c) and (d) illustrate the evolution of back stress and effective stress as a function of true tensile strain.

which constitutes approximately 66.8 % of the yield strength. This value significantly exceeds the 380.04 MPa observed in the L-PBF samples. Both the back-stress and effective stress in LMA-L-PBF samples exhibited a monotonic increase with tensile strain (Fig. 10(d)), consistently remaining higher than their L-PBF counterparts across the uniform strain range. The progressive rise in internal back stress, reaching up to 978.2 MPa before fracture, plays a pivotal role in dictating the flow stress of post-yield LMA-L-PBF samples, contributing approximately 67.0 % of the total flow stress during strain hardening. The observed enhancement in long-range back-stress hardening can be ascribed to the dynamic generation of dislocations in proximity to precipitates and heterostructures, while the pronounced short-range effective stress is a consequence of forest dislocation hardening stemming from a high dislocation density. The interplay between elevated back stress and effective stress collectively contributes to the remarkable strain hardening of LMA-L-PBF samples during tensile deformation. This significant improvement in strain hardening can be attributed to back-stress hardening associated with heterogeneous plastic deformation [40], ultimately leading to ultrahigh strength in MA-ASS due to the synergistic effects of these various hardening mechanisms.

5. Discussions

5.1. Deformation mechanisms in MA-ASS

To elucidate the unique strain hardening mechanism of the LMA-L-PBF samples, in-situ EBSD observations revealed that changes in grain characteristics—such as grain shape and size—are minimal (Fig. 11(a)).

The corresponding PF images illustrate variations in texture strength, indicating that as stretching progresses, the texture strength further diminishes. Fig. 11(b) presents a schematic representation of crystal rotation during the tensile process, which aids in understanding the decrease in texture strength with increasing tensile deformation (from 7.42 gradually decreasing to 5.57). The activation of slip systems facilitates lattice rotation, resulting in an increased percentage of LAGBs (Fig. 11(c) and (d); red arrows indicate that the emergence of LAGBs is closely associated with regions exhibiting elevated KAM values. Concurrently, the KAM value in fine-grain zones continuously increases compared to the initial state (Fig. 11(e) and (f)), accommodating further deformation [60]. This observation suggests that deformation within these regions primarily occurs through dislocation slip.

The microstructure of fine-grain zones was characterized across various stages of deformation. At an initial strain level of 1 % (Fig. 12(a) and (b)), the corresponding HRTEM image (Fig. 12(c)) indicates that dislocation slip is initiated with the emergence of extended stacking faults (SFs) (denoted by white dashed lines) on the primary {111} planes. As strain further increases, a larger number of grains activate fine, parallel stacking faults, leading to a higher density of SFs (Fig. 12 (d) and (e)). Notably, the microstructure of the MA-ASS alloy demonstrates inhomogeneity during deformation, particularly with high-density stacking faults appearing on two {111} slip systems near the fracture surface as stress intensifies during tensile loading until failure occurs. The HRTEM image illustrates the formation of a complex nanoscale network of intersecting stacking faults (Fig. 12(f)). Fig. 12(g) presents a schematic depiction of the proliferation of dislocations and SFs at varying levels of deformation. Diverse orientations of SFs were

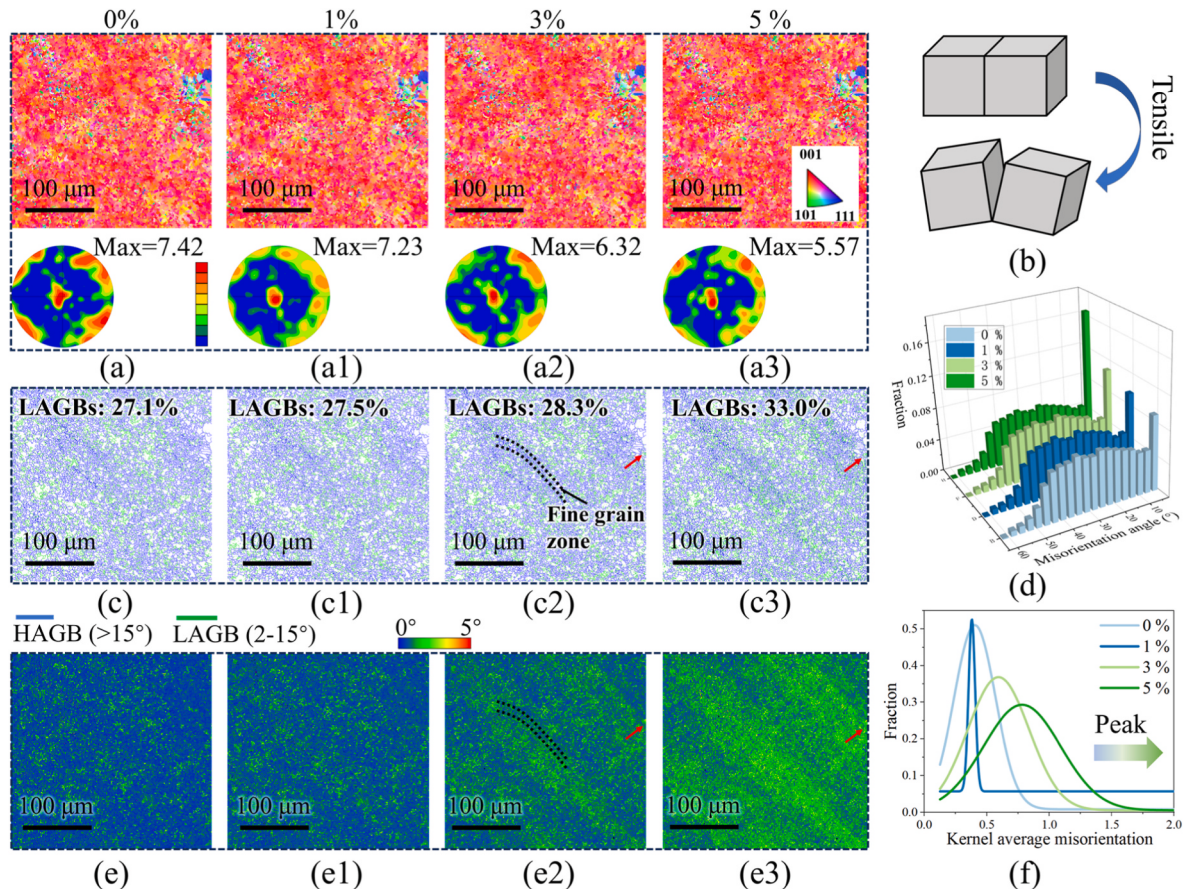


Fig. 11. Horizontal cross-sectional in-situ EBSD images of the MA-ASS under varying deformation states are presented, illustrating: (a-a3) the distribution of grain morphology at different scales and orientations. (b) A schematic diagram depicting crystal deflection, and (c-c3) boundaries defined by different misorientation angles. (d) Misorientation angle distributions across different deformation states. (e) The KAM map shows an increase in dislocation density of geometrically necessary dislocations compared to the as-built sample. (f) KAM angle distribution results.

identified within the grains, irrespective of their overall orientation. As strain continues to increase, the intersection of SFs proliferates significantly. Generally, the presence of SFs enhances both the strength and ductility of the material; however, excessive phase precipitation near the unit cell can induce local stress concentrations, thereby constraining additional elongation Fig. 12(h). The development of high-density Lomer-Cottrell (L-C) locks is critical in stabilizing the stacking fault network, as it effectively pins dislocation segments and prevents dislocation dissociation [61]. These L-C locks act not only as significant barriers to dislocation motion but also serve as Frank-Read sources, facilitating dislocation multiplication [62]. The formation of the SFs network and L-C locks is a dynamic process. Initially, their density is relatively low, which may limit their contribution to work hardening during the early stages of plastic deformation. However, as deformation progresses, the density of both the SFs network and L-C locks increases, thereby effectively delaying the onset of the decline in work hardening capacity. The generation of stacking faults and shear bands is intricately related to the activity and slip of partial dislocations at high-density fine-grain boundaries [63].

Three primary strategies have been employed to enhance the mechanical properties of alloys: (1) increasing resistance to dislocation slip, (2) strengthening interfaces, and (3) promoting uniform slip behavior. In this study, the first two strengthening mechanisms were achieved by increasing the precipitate phase and its density, alongside accelerating the cooling rate to form fine-grains. It is well-established that most metallurgical strengthening mechanisms inevitably lead to a reduction in ductility, a phenomenon known as the strength-ductility trade-off. This inverse relationship is mathematically described by Eq. (5) [64],

where E_c represents a constant value of strain energy density at the tip of the piled-up dislocations, and H_c denotes the critical spacing between the activated slip planes. This strength-ductility trade-off provides the theoretical framework for the high-strength steel fabricated using LMA-L-PBF. The introduction of Nb and Ti elements increases the stacking fault energy (SFE) in steels, thereby enhancing the strength of the FCC matrix while enabling additional elongation [65]. Notably, a higher density of slip bands within grains, coupled with more homogeneous shear deformation, results in improved plasticity [66]. However, despite the extensive proliferation of stacking faults within the austenitic matrix (Fig. 12(f)), the desired synergy between strength and ductility remains elusive. This could be attributed to the influence of precipitates on the uniformity of stacking fault structures.

$$\sigma_b = \sigma_0 + \frac{E_c}{H_c} \frac{1}{\varepsilon_U - \varepsilon_0} \quad \text{Eq. 5}$$

5.2. Strengthening mechanisms in LMA-L-PBF

The microstructure of the MA-ASS fabricated by LMA-L-PBF exhibits a hierarchical structure characterized by nanometric precipitates and multi-scale grains. It is essential to evaluate the contributions of various strengthening mechanisms to the overall material strength, with particular emphasis on precipitation strengthening and grain boundary strengthening. Fig. 13 presents TEM images alongside corresponding EDS data for both 316L SS and MA-ASS. In the case of 316L SS, the matrix is fortified by dislocation cells and the segregation of chromium at its boundaries. The diameter of precipitated particles in LMA-L-PBF samples is significantly larger than that in L-PBF samples. Conversely,

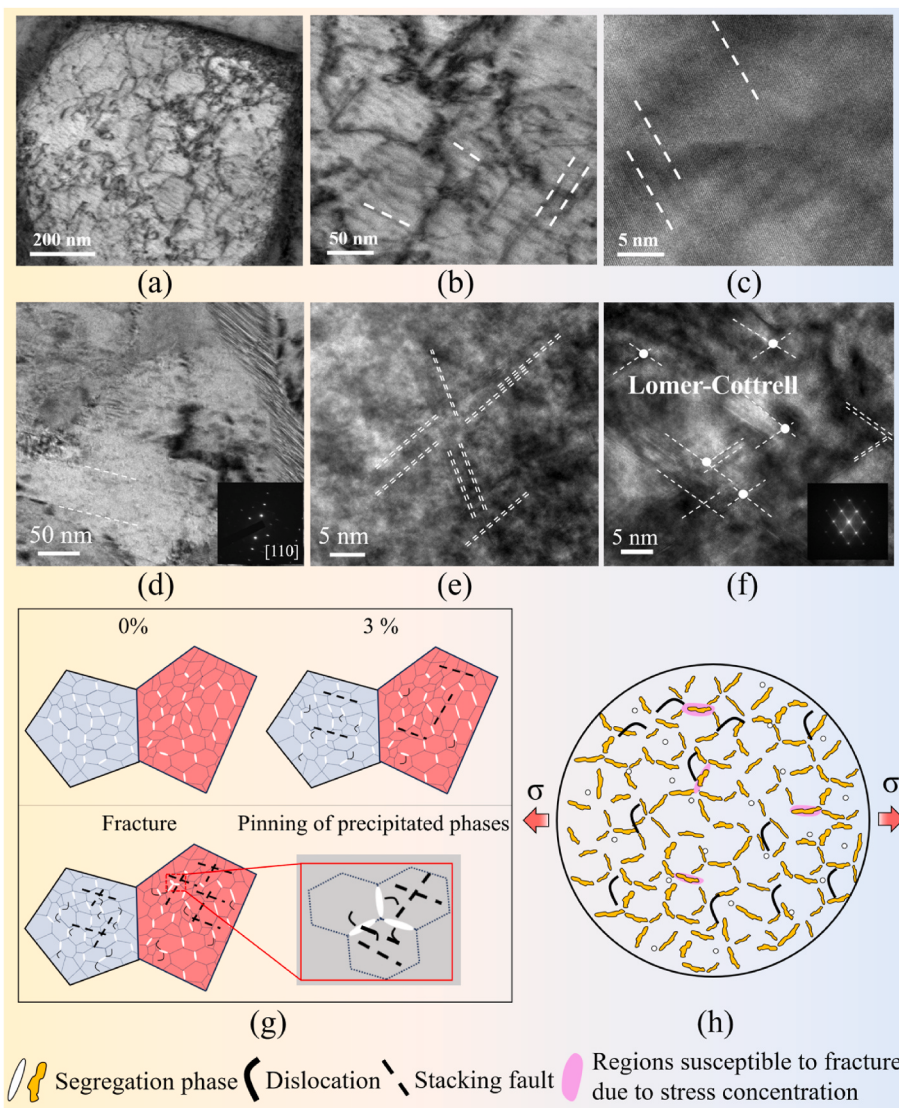


Fig. 12. The bright-field TEM images of MA-ASS fabricated by LMA-L-PBF at (a) 1 % tensile strain, (b) the corresponding enlarged image, and (c) the HRTEM images. (e) The inset at the bottom right of (d) the bright-field TEM images of MA-ASS at 3 % tensile strain is the corresponding SAED pattern. The HRTEM images of MA-ASS at (e) 5 % tensile strain and (f) fracture reveal the extensive formation of the SFs network (indicated by white dashed lines) across various {111} slip planes and within multiple dislocation cell structures. High-density L-C locks are observed near the fracture surface, with the corresponding FFT image shown in the inset. Schematic diagrams of (g) dislocations and SFs formed during deformation, and (h) stress concentration induced by segregation phases under applied strain. These schematic diagrams highlight the critical microstructural mechanisms governing plastic deformation and the initiation of mechanical failure in heterogeneous materials.

the sub-grain structure of MA-ASS is enhanced by precipitates that are rich in chromium and niobium. Precipitation of secondary phases is a widely employed method for strengthening metallic materials, commonly referred to as precipitation strengthening. The formation of a high density of precipitates results in a significant increase in mechanical strength. To estimate the dependence of strength on nanoprecipitated particles, the Orowan mechanism can be applied, which considers the dislocation pile-up at the interfaces of these particles [36]. The contribution to shear stress ($\Delta\tau$) and tensile strength ($\Delta\sigma$) due to the oxide particles can be expressed as follows [67]:

$$\Delta\tau = \frac{\mu b}{\lambda - D} \quad \text{Eq. 6}$$

where μ is the shear modulus (80 GPa), D is the particles' average diameter, λ is the average spacing, and b is the magnitude of Burger's vector (0.255 nm) of ordinary dislocations. The contribution to the tensile yield strength of the silicates ($\Delta\sigma$) can be described by

$$\Delta\sigma = M \cdot \Delta\tau$$

$$\text{Eq. 7}$$

The Taylor factor (M) is 3.01 for both MA-ASS and 316L SS fabricated via L-PBF, and 3.03 for MA-ASS fabricated by LMA-L-PBF, as measured using EBSD. The average diameter, spacing, and strength contributions of the particles are summarized in Table 4. Specifically, the strength contributions of nanoprecipitation for 316L SS and MA-ASS fabricated by L-PBF are 93.03 MPa and 127.76 MPa, respectively, while for 316L SS and MA-ASS fabricated by LMA-L-PBF, these contributions are 121.53 MPa and 161.48 MPa, respectively. The oxide particles in MA-ASS fabricated by LMA-L-PBF exhibit a smaller average diameter and a higher density, resulting in a significantly stronger strengthening effect.

The microstructure of the samples varies significantly, and it is essential to consider the strengthening effects arising from these refined microstructural changes. Fig. 14(a-c) presents the melt pool morphologies of 316L SS, MA-ASS fabricated by L-PBF, and MA-ASS fabricated

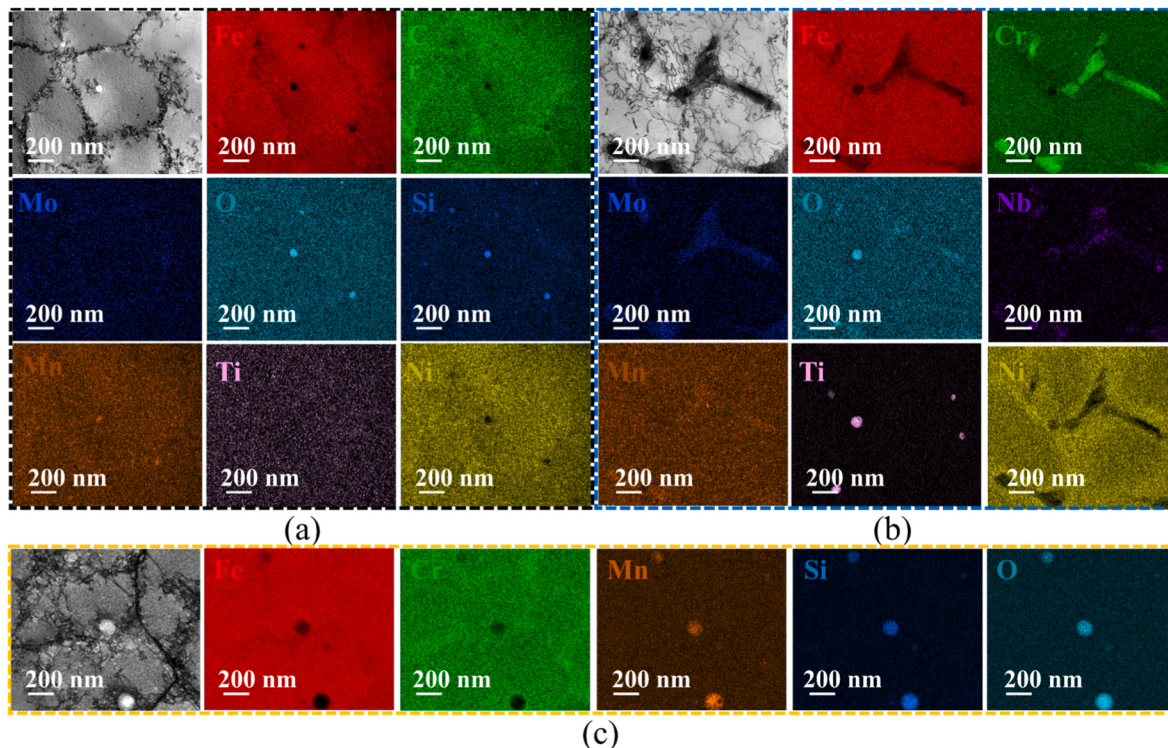


Fig. 13. The bright-field TEM and corresponding EDS images of (a) 316L SS and (b) MA-ASS fabricated by L-PBF and (c) 316L SS fabricated by LMA-L-PBF show segregation elements in the rapid solidification cellular boundaries with Mo, Cr, Nb, and O elements segregation. The 316L SS was covered with high-density dislocations, while those of MA-ASS were decorated with nanoscale precipitates.

Table 4

Calculated Orowan strengthening contributions of Ti-rich and Si-rich oxide particles.

| Process | Powder | Average diameter of oxide particles (nm) | Average spacing (nm) | $\Delta\tau$ (MPa) | $\Delta\sigma_{\text{Orowan}}$ (MPa) |
|-----------|---------|--|----------------------|--------------------|--------------------------------------|
| LMA-L-PBF | MA-AAS | 43.91 | 426.70 | 53.29 | 161.48 |
| | 316L SS | 122.63 | 651.18 | 38.60 | 116.95 |
| L-PBF | MA-AAS | 62.12 | 542.73 | 42.45 | 127.76 |
| | 316L SS | 78.23 | 738.27 | 30.91 | 93.03 |

by LMA-L-PBF, respectively. The melt pool edge of 316L SS is characterized by a neat, well-defined boundary and coarse grain structures that extend across multiple melt pools. In contrast, due to changes in undercooling induced by the Ti and Nb alloying elements, the melt pool edge of MA-ASS fabricated by L-PBF exhibits a more rapid cooling during solidification, leading to a refined microstructure. The inset in Fig. 14(b) presents EBSD images of MA-ASS fabricated by L-PBF, which further corroborate the optical observations. For additional microstructural details are refer to our previous work [21]. As the thermal conductivity of liquid Sn exceeds 64 W/mK at 573 K [68], whereas the thermal conductivities of the 316L SS powder (~ 0.3 W/mK) are less than 1/100th of the solid bulk thermal conductivities (~ 13.4 W/mK) the thermal conductivity [69], the use of liquid Sn alters the heat transfer mechanism during the process (Fig. 14(d)). According to our previous studies, compared to traditional powder bed fusion, liquid Sn accelerates heat exchange [70], leading to distinct microstructural features in the material. The low growth rate-to-cooling rate ratio (G/R) and high growth rate multiplied by cooling rate ($G \times R$) theoretically result in finer equiaxed crystals, as depicted in Fig. 14(e). For example, the microstructure of the MA-ASS fabricated by LMA-L-PBF at the melt pool edge is further refined. And the refined equiaxed crystals can be

observed at the bottom of the melt pool in LMA-L-PBF samples (Fig. 6(c)). The schematic illustration in Fig. 14(f) elucidates the synergistic interplay between material selection and processing strategies in achieving tailored microstructural refinement. During the LMA-L-PBF fabrication process, in addition to environmental and substrate-mediated heat dissipation, convective heat transfer of the liquid metal may serve as a pivotal factor for further enhancing the mechanical properties of precipitation-hardened alloys. These demonstrate the impact of thermal management within liquid metals on microstructural evolution during the additive manufacturing process.

At the same time, it is important to consider the differences in thermal conductivity and heat retention properties of liquid metals at varying temperatures, as these factors impact microstructure and performance. Fig. 15 illustrates the changes in grain size and mechanical properties of MA-ASS when the temperature of the liquid Sn is elevated to 673 K (400 °C). The EBSD image presented in Fig. 15(a) indicates that the fine-grain region has largely disappeared, with the average grain size increasing to 6.28 μm compared to the environment at 573 K (300 °C) shown in Fig. 15(b). Additionally, the proportion of HAGBs decreased to 72.2 % (Fig. 15(c)). At this elevated temperature, the yield strength and tensile strength of MA-ASS fabricated by LMA-L-PBF in liquid Sn at 673 K decreased to 791.05 ± 28.5 MPa and 1116.41 ± 36.75 MPa, respectively. However, the uniform elongation and elongation at break improved to 14.81 ± 1.77 % and 22.48 ± 2.11 % (Fig. 15(d)), which are double the values observed under the 300 °C liquid Sn forming conditions.

On one hand, the thermal conductivity of tin declines with rising temperature; on the other hand, an increased forming temperature promotes grain coarsening, although the average grain size remains smaller than that seen in MA-ASS fabricated by L-PBF. Notably, the strength remains within a high range, underscoring the capability of LMA-L-PBF to modulate microstructure and enhance material performance. These variations in grain size, driven by the increased temperature, significantly influence the strength-ductility transition of the

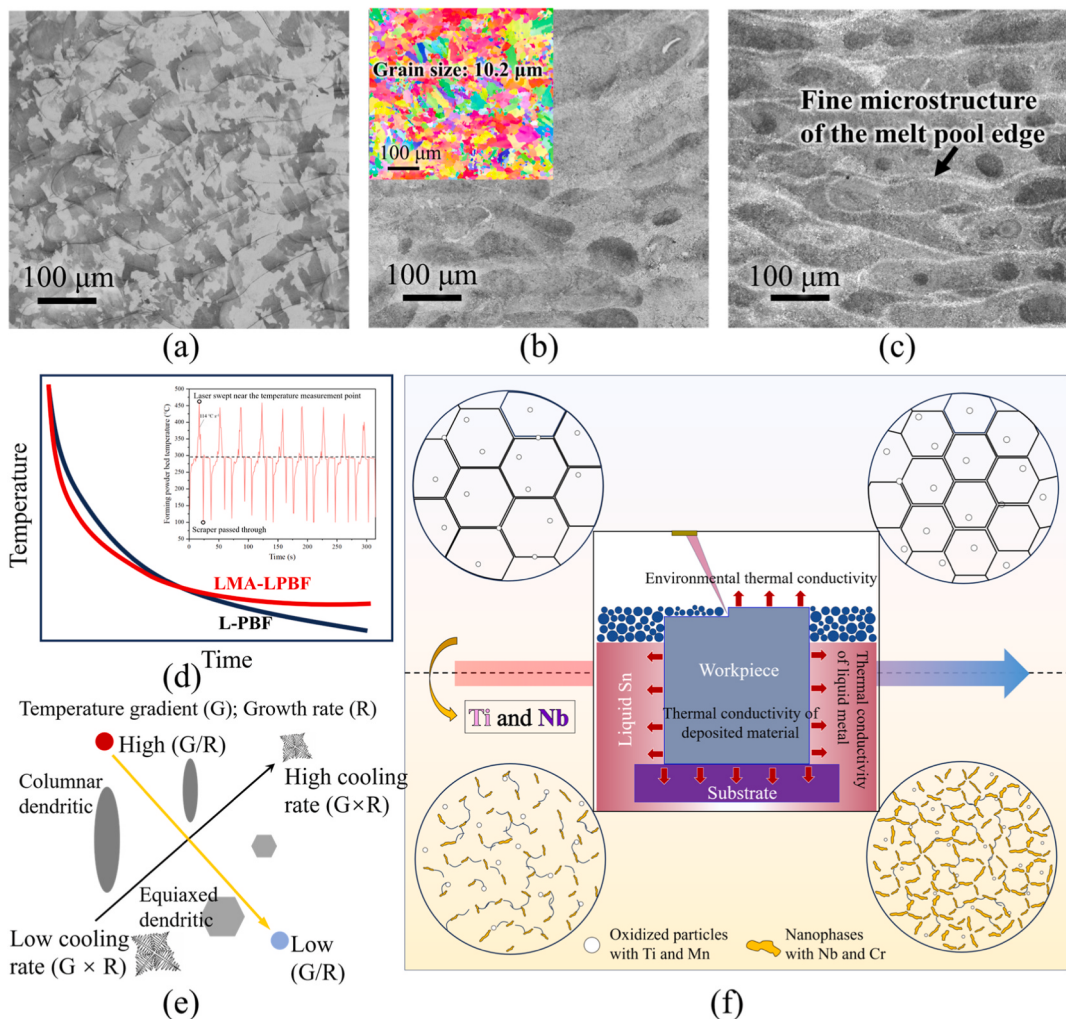


Fig. 14. Cross-sectional images of the melt pool of (a) 316L SS and (b) MA-ASS fabricated by L-PBF, and (c) MA-ASS fabricated by LMA-L-PBF. Corresponding vertical cross-sectional EBSD images of MA-ASS fabricated by L-PBF in (b). (d) Schematic diagram of the temperature and time relationship during the LMA-L-PBF and L-PBF forming processes, with the inset showing the real-time powder bed temperature measured during the LMA-L-PBF forming process. (e) The effect of temperature gradient and growth rate on grain size and morphology (adapted from Ref. [71]). (f) Schematic illustration of heat flow distribution and microstructural evolution during the LMA-L-PBF process.

material. Generally, the Hall–Petch relationship is employed to estimate the dependence of yield strength on grain size by considering dislocation pile-up against the phase interface [31]. The strength correlates with the Hall–Petch equation as follows:

$$\sigma_y = \sigma_0 + \frac{k_y}{\sqrt{d}} \quad \text{Eq. 8}$$

In this context, where k_y is the Hall–Petch coefficient. Referring to the works of Zhai et al. [44] and Han et al. [50], the experimental results were fitted using the Hall–Petch equation, yielding values of σ_0 and k_y as 396.19 MPa and 838.04 MPa^{0.5}, respectively. The strength contributions attributable to grain refinement in the MA-ASS samples fabricated by LMA-L-PBF at liquid Sn temperatures of 673 K and 573 K are determined to be 730.60 MPa and 826.09 MPa, respectively. While variations in processing conditions can lead to differences in the Hall–Petch parameters, these findings offer valuable insights for selecting optimal processing temperatures, adjusting grain sizes, and enhancing mechanical properties in LMA-L-PBF.

5.3. Evolution of heterogeneous microstructures

Compared to conventional L-PBF, the high thermal conductivity of

liquid Sn promotes grain refinement. Therefore, it is necessary to further compare the effects of different processing parameters in LMA-L-PBF on the evolution of heterogeneous structures, with a particular focus on the variation in the area fraction of fine-grained regions. Theoretically, grain size can be predicted using the interdependence model developed by St. John et al. [17] (Eq. (9)), which takes into account key parameters such as chemical composition, nucleant particle potency (ΔT_n), and particle spacing (x_{SD}).

$$d_{gs} = \frac{D \cdot z \cdot \Delta T_n}{R \cdot Q} + \frac{4.6 \cdot D}{R} \left(\frac{C_l^* - C_0}{C_l^*(1 - k)} \right) + x_{SD} \quad \text{Eq. 9}$$

Here, C_0 represents the solute concentration, D is the solute diffusion coefficient, R denotes the growth rate, k is the partition coefficient C_s/C_l , and C_l^* is the solute concentration at the solid–liquid interface. In the present study, it was found that the thermal undercooling effect induced by processing parameters plays a dominant role compared to the constitutional undercooling associated with heterogeneous nucleation from Nb and Ti additions. To clarify the influence of the remelted region area—determined by different values of E_0^* —on the evolution of heterogeneous microstructures, we primarily focus on how varying processing parameters affect the area fraction of fine-grained regions. Based on simulation results, Fig. 16(a) illustrates the changes in the melt pool

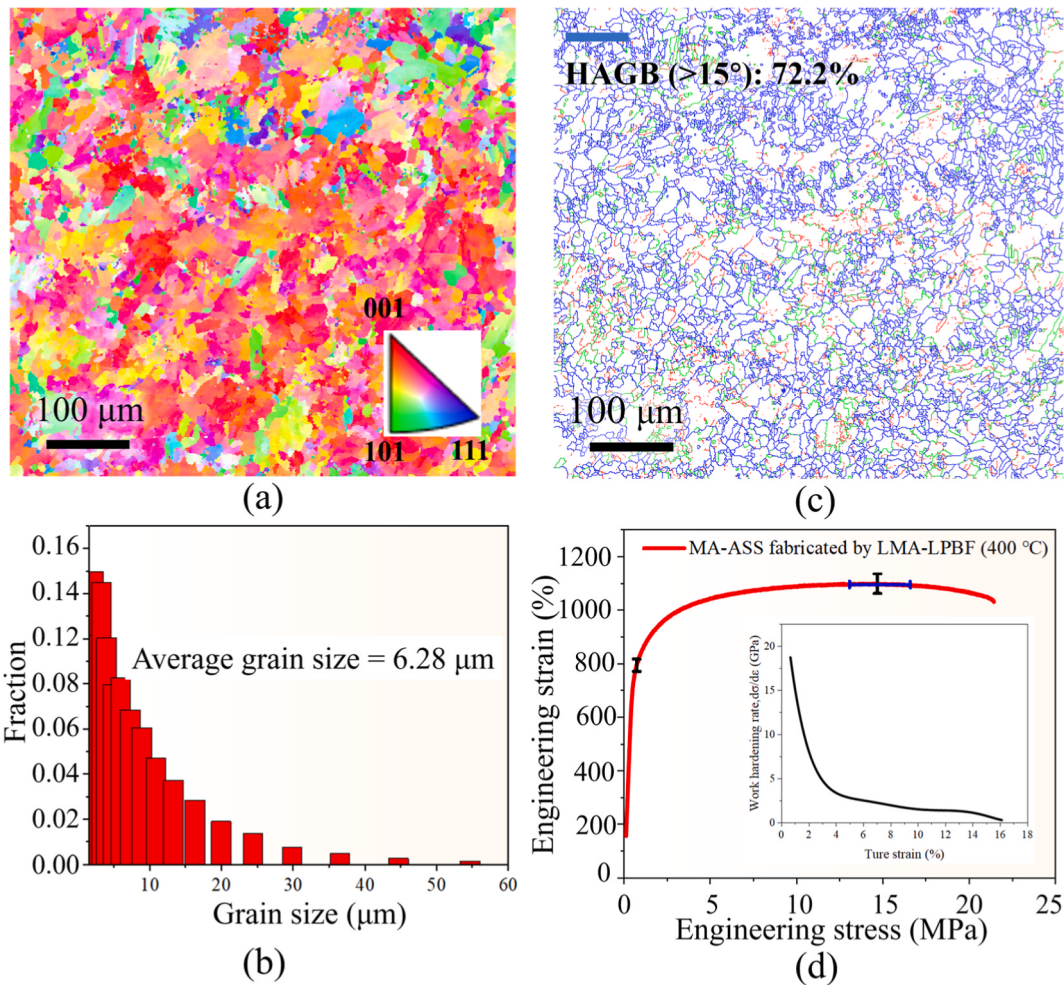


Fig. 15. Liquid Sn at 673K (400 °C), (a) grain distribution and orientation of MA-ASS (horizontal cross-section view), (b) average grain size results, (c) boundaries defined with different misorientation angles, and (d) tensile engineering and the corresponding strain hardening rate and true strain relations (inset).

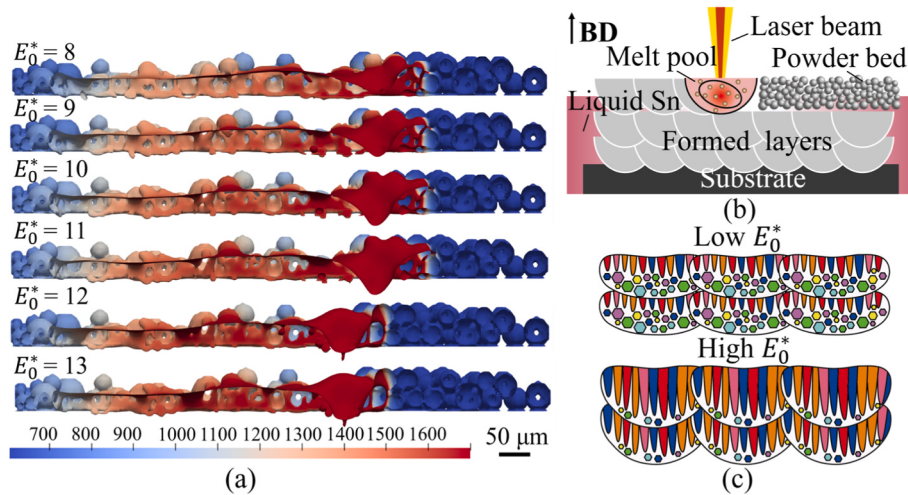


Fig. 16. (a) Morphologies of the melt pool and corresponding temperature profiles under different heat inputs, as obtained by numerical simulation. Schematic illustration of (b) LMA-L-PBF process, (c) variation of E_0^* indicates its influence on the melt pool morphology and solidification rate of multi-layer evolution, which in turn affects the distribution of grain sizes.

under different heat inputs for LMA-L-PBF; details of the simulation methodology are provided in the Supplementary Materials. During single-layer deposition, increases in E_0^* lead to significant changes in the

depth and width of the melt pool. At $E_0^* = 13$, the melt pool exhibits a marked enlargement compared to lower E_0^* values. The choice of processing parameters not only dictates the total heat input per unit time to

the powder near the laser source, but also governs the extent of the region subjected to repeated remelting. Consequently, the laser heat during the build process affects both newly formed and previously solidified layers; differences in remelted area result in variations in the growth rates of nascent and existing grains, as well as in solute redistribution. Fig. 16(b and c) illustrate the multi-layer solidification process in LMA-L-PBF, including schematic depictions of the solid–liquid interface and grain nucleation. Typically, in regions where the temperature gradient at the solid–liquid interface is steep and where effective constitutional undercooling is insufficient, columnar grains tend to grow along the direction of the temperature gradient. During multilayer additive manufacturing, a high E_0^* value generates a larger melt pool within the powder bed, which enhances thermal diffusion in the molten region. This elevated average pool temperature and reduced cooling rate produce a steeper thermal gradient, promoting the growth of larger grains. Furthermore, the expansion of the remelted area helps to minimize elemental segregation, resulting in a more homogeneous microstructure and, ultimately, the coarsening of previously formed grains.

Conversely, when E_0^* is low, the heat-affected zone of the already solidified layer remains small, effectively limiting the extent to which fine grains in a single deposited layer are remelted during subsequent deposition (Fig. 16(c)). This provides additional opportunities for heterogeneous grain formation within the melt pool. Further simulation results, as detailed in the Supplementary Figs. 7–9, confirm that the cooling rate under excessive heat input is indeed lower than that observed under lower heat input conditions in both L-PBF and LMA-L-PBF processes. The liquid Sn, due to its high thermal conductivity and fluidity, significantly reduces the cooling time within the melt pool of the LMA-L-PBF process. Increasing the E_0^* results in a reduction in cooling rates. This slower cooling process allows for grain growth, leading to larger grains in areas with steep thermal gradients. Conversely, at lower energy densities, smaller melt pools are formed with faster cooling rates, promoting finer grain structures as the solidification occurs more rapidly. It should be noted, however, that lower laser heat input leads to smaller melt pools, and the rapid solidification of these pools is conducive to the formation of more stable dendritic structures at high cooling rates, reducing the time required for equiaxed nucleation. Changes in melt pool morphology and solidification rate, combined with potential local segregation of microalloying elements, promote the formation of heterogeneous microstructure. Therefore, optimizing process parameters within an appropriate heat input window—where the cooling rate is slow enough to suppress dendritic or columnar growth, yet rapid enough to prevent excessive grain coarsening—offers a viable strategy for achieving ideal microstructures in the in-situ field coupling process.

6. Conclusions

This study describes a novel process technology using liquid metal to assist laser powder bed fusion. The principles underlying liquid metal-assisted laser powder bed fusion for tuning the microstructure and mechanical properties of materials were presented, expanding the controllable process window in additive manufacturing. Using austenitic stainless steels as the forming objects, the new process demonstrates different material characteristics than conventional L-PBF, obtaining an ultrahigh strength with a heterogeneous microstructure state. Key findings and conclusions are summarized as follows.

- Under the assistance of liquid metal, controlling the laser energy density facilitates fine-grain nucleation, enabling the formation of distinct heterogeneous grain structures. At an energy density fall near the $E_0^* \sim 10$ isopleth line, a dense microstructure with enlarged fine-grain regions was achieved through precise tuning of processing parameters.

- The precipitation of numerous Ti, Nb, and Cr-rich nanoparticles leads to changes in the solute concentration within austenitic stainless steel. This results in local grain refinement, particularly in regions with faster cooling rates in the melt pool. And the nanometric precipitates pin the grain boundaries and dislocations, forming the “hammer-chain” dislocation cell wall structure.
- MA-ASS fabricated by LMA-L-PBF exhibits a heterogeneous microstructure spanning nanometer to micrometer scales. Benefiting from grain refinement, precipitation hardening and dislocation strengthening, it achieves a yield strength exceeding 1.1 GPa and an ultimate tensile strength of 1.5 GPa, while maintaining a uniform elongation of 7 %. This demonstrates the potential applicability of liquid metal-assisted additive manufacturing principles for in-situ reinforced precipitation-hardened alloys.
- Due to dislocation activities (e.g., slip, stacking, and dislocation entanglement), MA-ASS exhibits an unusual strain hardening mechanism. And the accumulation of geometrically necessary dislocations at heterogeneous interfaces, grain boundaries, dislocation cell walls, and incoherent precipitate boundaries contributes to the elevated back stress observed in MA-ASS fabricated via LMA-L-PBF.

Unlike the other powder-based additive manufacturing techniques, this novel technology replaces the conventional passively stacked powder bed with a thin layer of powder floating on liquid metal. This innovation not only allows for more precise control over the forming environment's temperature but also reduces powder consumption shall be beneficial to the broader industrial community, which increasingly values cost-effectiveness and sustainability, paving the way for the production of components that require a balance of strength and costs. Moreover, the findings presented in this study could extend beyond the specific case of austenitic stainless steels. The potential to redefine how microstructures are engineered provides a new route for the precise manipulation of material properties. The control of grain size, precipitation, and dislocation strengthening mechanisms could be leveraged to enhance materials used in aerospace, automotive, and biomedical sectors, where the combination of high strength and toughness is paramount.

Although the proposed LMA-L-PBF technology has produced promising results, it is important to acknowledge its limitations. For example, under a high temperature (>500 °C), liquid tin may react perceptibly with certain alloys, i.e., steels, superalloys, etc., leading to material degradation or corrosion, which impede the material forming process and even damage the equipment (as they are manufactured with steels in most cases). To mitigate these potential issues, several strategies should be considered. One approach is to apply a protective coating to the forming tank to effectively isolate it from direct contact with liquid tin during the manufacturing process. Additionally, the effect of the in-situ thermal field in the LAM-L-PBF process might be more intricate than what this study reveals, particularly when applied to different material systems. Based on material properties—such as titanium alloys exhibiting lower thermal conductivity and superior resistance to tin corrosion, while certain aluminum alloys demonstrate varying crack sensitivity at different temperatures—the interactions between these characteristics and the LAM-L-PBF process require additional experimental validation.

CRediT authorship contribution statement

Xiaoyu Liang: Writing – original draft, Writing – review & editing, Methodology, Funding acquisition, Conceptualization. **Yurong Wang:** Writing – original draft, Methodology, Investigation, Data curation, Conceptualization. **Wei Liu:** Investigation, Data curation. **Buwei Xiao:** Investigation, Data curation. **Qingze Liu:** Data curation. **Yizhuo Sun:** Data curation. **Pengcheng Lv:** Data curation. **Huabei Peng:** Data curation. **Jun Zhou:** Data curation. **Lei Zhang:** Data curation. **Feng Lin:** Writing – review & editing, Supervision, Funding acquisition, Conceptualization.

Declaration of competing interest

The authors declare that they have no known competing financial interests or personal relationships that could have appeared to influence the work reported in this paper.

Acknowledgements

The authors acknowledge support from the National Natural Science Foundation of China (NSFC) for the Continuing Funding Projects: 52250009, National Natural Science Foundation of China (NSFC) for the Original Exploration Program Projects: 52050110 and the Youth Funding from the Department of Mechanical Engineering, Tsinghua University.

Appendix A. Supplementary data

Supplementary data to this article can be found online at <https://doi.org/10.1016/j.ijmachtools.2025.104334>.

Data availability

Data will be made available on request.

References

- [1] T. Song, Z. Chen, X. Cui, S. Lu, H. Chen, H. Wang, T. Dong, B. Qin, K.C. Chan, M. Brandt, X. Liao, S.P. Ringer, M. Qian, Strong and ductile titanium-oxygen-iron alloys by additive manufacturing, *Nature* 618 (2023) 63–68, <https://doi.org/10.1038/s41586-023-05952-6>.
- [2] T. Zhang, Z. Huang, T. Yang, H. Kong, J. Luan, A. Wang, D. Wang, W. Kuo, Y. Wang, C.-T. Liu, *In situ* design of advanced titanium alloy with concentration modulations by additive manufacturing, *Science* 374 (2021) 478–482, <https://doi.org/10.1126/science.abj3770>.
- [3] K.M. Bertsch, G. Merit de Bellefon, B. Kuehl, D.J. Thoma, Origin of dislocation structures in an additively manufactured austenitic stainless steel 316L, *Acta Mater.* 199 (2020) 19–33, <https://doi.org/10.1016/j.actamat.2020.07.063>.
- [4] B. Zheng, Y. Zhou, J.E. Smigajesky, J.M. Schoenung, E.J. Lavernia, Thermal behavior and microstructural evolution during laser deposition with laser-engineered net shaping: part I. Numerical calculations, *Metall. Mater. Trans.* 39 (2008) 2228–2236, <https://doi.org/10.1007/s11661-008-9557-7>.
- [5] G.M. Karthik, H.S. Kim, Heterogeneous aspects of additive manufactured metallic parts: a review, *Met. Mater. Int.* 27 (2021) 1–39, <https://doi.org/10.1007/s12540-020-00931-2>.
- [6] C. Chen, Z. Zhang, Y. Cai, Y. Liu, H. Chen, Research and development status of in situ field assisted laser additive manufacturing: a review, *Opt Laser. Technol.* 181 (2025) 111700, <https://doi.org/10.1016/j.optlastec.2024.111700>.
- [7] C. Tan, R. Li, J. Su, D. Du, Y. Du, B. Attard, Y. Chew, H. Zhang, E.J. Lavernia, Y. Fautrelle, J. Teng, A. Dong, Review on field assisted metal additive manufacturing, *Int. J. Mach. Tool Manufact.* 189 (2023) 104032, <https://doi.org/10.1016/j.ijmachtools.2023.104032>.
- [8] S. Munusamy, J. Jerald, Effect of in-Situ intrinsic heat treatment in metal additive manufacturing: a comprehensive review, *Met. Mater. Int.* 29 (2023) 3423–3441, <https://doi.org/10.1007/s12540-023-01462-2>.
- [9] G. Huang, B. Li, J. Zhang, F. Xuan, Multi-material laser powder bed fusion additive manufacturing of dual-phase laminated heterostructure of Cantor high-entropy alloy and Martensite steel for overcoming strength-ductility trade-off, *Addit. Manuf.* 97 (2025) 104618, <https://doi.org/10.1016/j.addma.2024.104618>.
- [10] Y.M. Wang, T. Voisin, J.T. McKeown, J. Ye, N.P. Calta, Z. Li, Z. Zeng, Y. Zhang, W. Chen, T.T. Roehling, R.T. Ott, M.K. Santala, Philip J. Depond, M.J. Matthews, A. V. Hamza, T. Zhu, Additively manufactured hierarchical stainless steels with high strength and ductility, *Nat. Mater.* 17 (2018) 63–71, <https://doi.org/10.1038/nmat5021>.
- [11] T.H. Fang, W.L. Li, N.R. Tao, K. Lu, Revealing extraordinary intrinsic tensile plasticity in gradient nano-grained copper, *Science* 331 (2011) 1587–1590, <https://doi.org/10.1126/science.120017>.
- [12] Y. Wei, Y. Li, L. Zhu, Y. Liu, X. Lei, G. Wang, Y. Wu, Z. Mi, J. Liu, H. Wang, H. Gao, Evading the strength-ductility trade-off dilemma in steel through gradient hierarchical nanotwins, *Nat. Commun.* 5 (2014) 3580, <https://doi.org/10.1038/ncomms4580>.
- [13] F.K. Yan, G.Z. Liu, N.R. Tao, K. Lu, Strength and ductility of 316L austenitic stainless steel strengthened by nano-scale twin bundles, *Acta Mater.* 60 (2012) 1059–1071, <https://doi.org/10.1016/j.actamat.2011.11.009>.
- [14] Y.B. Lei, Z.B. Wang, B. Zhang, Z.P. Luo, J. Lu, K. Lu, Enhanced mechanical properties and corrosion resistance of 316L stainless steel by pre-forming a gradient nanostructured surface layer and annealing, *Acta Mater.* 208 (2021) 116773, <https://doi.org/10.1016/j.actamat.2021.116773>.
- [15] S.P. Murray, K.M. Pusch, A.T. Polonsky, C.J. Torbet, G.G.E. Seward, N. Zhou, S.A. J. Forsik, P. Nandwana, M.M. Kirkha, R.R. Dehoff, W.E. Slye, T.M. Pollock, A defect-resistant Co–Ni superalloy for 3D printing, *Nat. Commun.* 11 (2020) 4975, <https://doi.org/10.1038/s41467-020-18775-0>.
- [16] T. DebRoy, H.L. Wei, J.S. Zuback, T. Mukherjee, J.W. Elmer, J.O. Milewski, A. M. Beese, A. Wilson-Heid, A. De, W. Zhang, Additive manufacturing of metallic components – process, structure and properties, *Prog. Mater. Sci.* 92 (2018) 112–224.
- [17] D.H. StJohn, M. Qian, M.A. Easton, P. Cao, The Interdependence Theory: the relationship between grain formation and nucleant selection, *Acta Mater.* 59 (2011) 4907–4921, <https://doi.org/10.1016/j.actamat.2011.04.035>.
- [18] M. Bermingham, D. StJohn, M. Easton, L. Yuan, M. Dargusch, Revealing the mechanisms of grain nucleation and formation during additive manufacturing, *JOM* 72 (2020) 1065–1073, <https://doi.org/10.1007/s11837-020-04019-5>.
- [19] S.B. Han, Y.S. Lee, S.H. Park, H. Song, Ti-containing 316L stainless steels with excellent tensile properties fabricated by directed energy deposition additive manufacturing, *Mater. Sci. Eng., A* 862 (2023) 144414.
- [20] L. Tan, J.D. Poplawsky, Y. Yang, Effects of niobium and tantalum on the microstructure and strength of ferritic-martensitic steels, *Mater. Sci. Eng., A* 807 (2021) 140900.
- [21] Y. Wang, B. Xiao, X. Liang, H. Peng, J. Zhou, F. Lin, Strengthened microstructure and mechanical properties of austenitic 316L stainless steels by grain refinement and solute segregation, *J. Mater. Res. Technol.* 34 (2025) 552–565.
- [22] F.J. Alamos, J. Schiltz, K. Kozlovsky, R. Attardo, C. Toronto, T. Pelletiers, S. R. Schmid, Effect of powder reuse on mechanical properties of Ti-6Al-4V produced through selective laser melting, *Int. J. Refract. Metals Hard Mater.* 91 (2020) 105273.
- [23] M. Lutter-Günther, C. Gebbe, T. Kamps, C. Seidel, G. Reinhart, Powder recycling in laser beam melting: strategies, consumption modeling and influence on resource efficiency, *Prod. Eng.* 12 (2018) 377–389.
- [24] Y. Wang, W. Liu, B. Xiao, X. Liang, P. Lv, J. Zhou, F. Lin, Wettability of Sn alloys at metal interfaces: metal surface treatment, interfacial temperature control and elemental modification, *Surf. Coatings. Technol.* 502 (2025) 131991.
- [25] I. Sari, L. Hachani, A. Kharicha, Y. Fautrelle, B. Pichat, K. Zaidat, 3D numerical simulation and experimental investigation of pure tin solidification under natural and forced convection, *Int. J. Therm. Sci.* 164 (2021) 106900.
- [26] A. Passerone, E. Ricci, R. Sangiorgi, Influence of oxygen contamination on the surface tension of liquid tin, *J. Mater. Sci.* 25 (1990) 4266–4272.
- [27] M. Thomas, G.J. Baxter, I. Todd, Normalised model-based processing diagrams for additive layer manufacture of engineering alloys, *Acta Mater.* 108 (2016) 26–35.
- [28] J. Ren, Y. Zhang, D. Zhao, Y. Chen, S. Guan, Y. Liu, L. Liu, S. Peng, F. Kong, J. D. Poplawsky, G. Gao, T. Voisin, K. An, Y.M. Wang, K.Y. Xie, T. Zhu, W. Chen, Strong yet ductile nanolamellar high-entropy alloys by additive manufacturing, *Nature* 608 (2022) 62–68.
- [29] Standard Practice for Determining the Inclusion or Second-Phase Constituent Content of Metals by Automatic Image Analysis, ASTM-E1245 (2008).
- [30] J.I. Dickson, Jr. Boutin, L. Handfield, A comparison of two simple methods for measuring cyclic internal and effective stresses, *Mater. Sci. Eng.* 64 (1984), [https://doi.org/10.1016/0025-5416\(84\)90083-1](https://doi.org/10.1016/0025-5416(84)90083-1).
- [31] A. Misra, J.P. Hirth, R.G. Hoagland, Length-scale-dependent deformation mechanisms in incoherent metallic multilayered composites, *Acta Mater.* 53 (2005) 4817–4824, <https://doi.org/10.1016/j.actamat.2005.06.025>.
- [32] Z. Zhou, J. Lv, M. Gui, W. Yang, New insights into annealing induced hardening and deformation mechanisms in a selective laser melting austenitic stainless steel 316L, *Int. J. Plast.* 178 (2024) 104008, <https://doi.org/10.1016/j.ijplas.2024.104008>.
- [33] T. Zhang, Z. Huang, T. Yang, H. Kong, J. Luan, A. Wang, D. Wang, W. Kuo, Y. Wang, C.-T. Liu, In situ design of advanced titanium alloy with concentration modulations by additive manufacturing, *Science* 374 (2021) 478–482, <https://doi.org/10.1126/science.abj3770>.
- [34] D. Du, L. Wang, A. Dong, W. Yan, G. Zhu, B. Sun, Promoting the densification and grain refinement with assistance of static magnetic field in laser powder bed fusion, *Int. J. Mach. Tool Manufact.* 183 (2022) 103965, <https://doi.org/10.1016/j.ijmachtools.2022.103965>.
- [35] M.R. Jandaghi, H. Pouraliakbar, S.H. Shim, V. Fallah, S.I. Hong, M. Pavese, In-situ alloying of stainless steel 316L by co-inoculation of Ti and Mn using LPBF additive manufacturing: microstructural evolution and mechanical properties, *Mater. Sci. Eng., A* 857 (2022) 144114, <https://doi.org/10.1016/j.msea.2022.144114>.
- [36] K. Ma, H. Wen, T. Hu, T.D. Topping, D. Isheim, D.N. Seidman, E.J. Lavernia, J. M. Schoenung, Mechanical behavior and strengthening mechanisms in ultrafine grain precipitation-strengthened aluminum alloy, *Acta Mater.* 62 (2014) 141–155, <https://doi.org/10.1016/j.actamat.2013.09.042>.
- [37] S. Wei, C. Hutchinson, U. Ramamurthy, Mesostructure engineering in additive manufacturing of alloys, *Scr. Mater.* 230 (2023) 115429, <https://doi.org/10.1016/j.scriptamat.2023.115429>.
- [38] H. Ueno, K. Kakihata, Y. Kaneko, S. Hashimoto, A. Vinogradov, Enhanced fatigue properties of nanostructured austenitic SUS 316L stainless steel, *Acta Mater.* 59 (2011) 7060–7069, <https://doi.org/10.1016/j.actamat.2011.07.061>.
- [39] X. Wu, P. Jiang, L. Chen, F. Yuan, Y.T. Zhu, Extraordinary strain hardening by gradient structure, *Proc. Natl. Acad. Sci.* 111 (2014) 7197–7201, <https://doi.org/10.1073/pnas.1324069111>.
- [40] R. Casati, J. Lemke, M. Vedani, Microstructure and fracture behavior of 316L austenitic stainless steel produced by selective laser melting, *J. Mater. Sci. Technol.* 32 (2016) 738–744, <https://doi.org/10.1016/j.jmst.2016.06.016>.
- [41] S. Bahl, S. Mishra, K.U. Yazar, I.R. Kola, K. Chatterjee, S. Suwas, Non-equilibrium microstructure, crystallographic texture and morphological texture synergistically

- result in unusual mechanical properties of 3D printed 316L stainless steel, *Addit. Manuf.* 28 (2019) 65–77, <https://doi.org/10.1016/j.addma.2019.04.016>.
- [42] Y. Liu, J. Sun, Y. Fu, B. Xu, B. Li, S. Xu, P. Huang, J. Cheng, Y. Han, J. Han, G. Wu, Tuning strength-ductility combination on selective laser melted 316L stainless steel through gradient heterogeneous structure, *Addit. Manuf.* 48 (2021) 102373, <https://doi.org/10.1016/j.addma.2021.102373>.
- [43] P. Kumar, R. Jayaraj, J. Suryawanshi, U.R. Satwik, J. McKinnell, U. Ramamurty, Fatigue strength of additively manufactured 316L austenitic stainless steel, *Acta Mater.* 199 (2020) 225–239, <https://doi.org/10.1016/j.actamat.2020.08.033>.
- [44] W. Zhai, W. Zhou, S.M.L. Nai, Grain refinement of 316L stainless steel through in-situ alloying with Ti in additive manufacturing, *Mater. Sci. Eng., A* 840 (2022) 142912, <https://doi.org/10.1016/j.msea.2022.142912>.
- [45] D. Riabov, M. Rashidi, E. Hryha, S. Bengtsson, Effect of the powder feedstock on the oxide dispersion strengthening of 316L stainless steel produced by laser powder bed fusion, *Mater. Char.* 169 (2020) 110582, <https://doi.org/10.1016/j.matchar.2020.110582>.
- [46] Y. Li, T. Krajinák, P. Podaný, J. Veselý, J. Džugan, Thermal stability of dislocation structure and its effect on creep property in austenitic 316L stainless steel manufactured by directed energy deposition, *Mater. Sci. Eng., A* 873 (2023) 144981, <https://doi.org/10.1016/j.msea.2023.144981>.
- [47] K. Xu, B. Li, C. Jiang, Adjusting microstructure and improving mechanical property of additive manufacturing 316L based on process optimization, *Mater. Sci. Eng., A* 870 (2023) 144824, <https://doi.org/10.1016/j.msea.2023.144824>.
- [48] Y. Zhong, Z. Zheng, J. Li, C. Wang, Effect of in-situ transverse magnetic field on microstructure, mechanical properties and corrosion resistance of the directed energy deposited 316L stainless steel, *Addit. Manuf.* 68 (2023) 103508, <https://doi.org/10.1016/j.addma.2023.103508>.
- [49] M. Ziętala, T. Durekko, M. Polański, I. Kunce, T. Płociński, W. Zieliński, M. Łazińska, W. Stępniewski, T. Czujko, K.J. Kurzydłowski, Z. Bojar, The microstructure, mechanical properties and corrosion resistance of 316L stainless steel fabricated using laser engineered net shaping, *Mater. Sci. Eng., A* 677 (2016) 1–10, <https://doi.org/10.1016/j.msea.2016.09.028>.
- [50] S.B. Han, H. Song, S.H. Park, Improvement of tensile properties through Nb addition and heat treatment in additively manufactured 316L stainless steel using directed energy deposition, *J. Mater. Res. Technol.* 29 (2024) 4806–4821, <https://doi.org/10.1016/j.jmrt.2024.02.184>.
- [51] I.A. Segura, J. Mireles, D. Bermudez, C.A. Terrazas, L.E. Murr, K. Li, V.S.Y. Injeti, R.D.K. Misra, R.B. Wicker, Characterization and mechanical properties of cladded stainless steel 316L with nuclear applications fabricated using electron beam melting, *J. Nucl. Mater.* 507 (2018) 164–176, <https://doi.org/10.1016/j.jnucmat.2018.04.026>.
- [52] S. Guo, J. Xu, J. Gu, Y. Peng, Q. Zhou, K. Wang, Effect of cellular structure on the mechanical properties of 316L stainless steel fabricated by EBF³, *J. Mater. Res. Technol.* 25 (2023) 5469–5482, <https://doi.org/10.1016/j.jmatprot.2023.07.024>.
- [53] C. Wang, X. Tan, E. Liu, S.B. Tor, Process parameter optimization and mechanical properties for additively manufactured stainless steel 316L parts by selective electron beam melting, *Mater. Des.* 147 (2018) 157–166, <https://doi.org/10.1016/j.matdes.2018.03.035>.
- [54] K. Xu, M. Yu, S. Huang, H. Tian, L. Mao, X. Liu, D. Zheng, H. Gao, D. Zhao, B. Li, Strengthening the additively manufactured 316L stainless steel by adding Al, *Mater. Lett.* 357 (2024) 135529, <https://doi.org/10.1016/j.matlet.2023.135529>.
- [55] S.-H. Kim, H. Kim, N.J. Kim, Brittle intermetallic compound makes ultrastrong low-density steel with large ductility, *Nature* 518 (2015) 77–79, <https://doi.org/10.1038/nature14144>.
- [56] S. Ramtani, H.Q. Bui, G. Dirras, A revisited generalized self-consistent polycrystal model following an incremental small strain formulation and including grain-size distribution effect, *Int. J. Eng. Sci.* 47 (2009) 537–553, <https://doi.org/10.1016/j.ijengsci.2008.09.005>.
- [57] K. Lu, F.K. Yan, H.T. Wang, N.R. Tao, Strengthening austenitic steels by using nanotwinned austenitic grains, *Scr. Mater.* 66 (2012) 878–883, <https://doi.org/10.1016/j.scriptamat.2011.12.044>.
- [58] Y. Zhu, K. Ameyama, P.M. Anderson, I.J. Beyerlein, H. Gao, H.-S. Kim, E. J. Lavernia, S.N. Mathaudhu, H. Mughrabi, R.O. Ritchie, N. Tsuji, X. Zhang, X.J.M. R.L. Wu, Heterostructured materials: superior properties from hetero-zone interaction, *Materials Research Letters* 9 (2020) 1–31, <https://doi.org/10.1080/21663831.2020.1796836>.
- [59] J.I. Dickson, J. Boutin, L. Handfield, A comparison of two simple methods for measuring cyclic internal and effective stresses, *Mater. Sci. Eng.* 64 (1984) L7–L11, [https://doi.org/10.1016/0025-5416\(84\)90083-1](https://doi.org/10.1016/0025-5416(84)90083-1).
- [60] H. Mughrabi, Dislocation wall and cell structures and long-range internal stresses in deformed metal crystals, *Acta Metall.* 31 (1983) 1367–1379, [https://doi.org/10.1016/0001-6160\(83\)90007-X](https://doi.org/10.1016/0001-6160(83)90007-X).
- [61] X.L. Wu, Y.T. Zhu, Y.G. Wei, Q. Wei, Strong strain hardening in nanocrystalline nickel, *Phys. Rev. Lett.* 103 (2009) 205504, <https://doi.org/10.1103/PhysRevLett.103.205504>.
- [62] S. Chen, H.S. Oh, B. Gludovatz, S.J. Kim, E.S. Park, Z. Zhang, R.O. Ritchie, Q. Yu, Real-time observations of TRIP-induced ultrahigh strain hardening in a dual-phase CrMnFeCoNi high-entropy alloy, *Nat. Commun.* 11 (2020) 826, <https://doi.org/10.1038/s41467-020-14641-1>.
- [63] M.A. Meyers, K.K. Chawla, *Mechanical Behavior of Materials*, 2 ed., Cambridge University Press, Cambridge, 2008.
- [64] X.T. Li, R. Liu, J.P. Hou, Z.J. Zhang, Z.F. Zhang, Trade-off model for strength-ductility relationship of metallic materials, *Acta Mater.* 289 (2025) 120942, <https://doi.org/10.1016/j.actamat.2025.120942>.
- [65] A. Suzuki, H. Inui, T.M. Pollock, L₁₂-Strengthened cobalt-base superalloys, *Annu. Rev. Mater. Res.* 45 (2015) 345–368, <https://doi.org/10.1146/annurev-matsci-070214-021043>.
- [66] T. Okita, Y. Yang, J. Hirabayashi, M. Itakura, K. Suzuki, Effects of stacking fault energy on defect formation process in face-centered cubic metals, *Philos. Mag.* 96 (15) (2016) 1579–1597, <https://doi.org/10.1080/14786435.2016.1171415>.
- [67] J. Hu, B. Chen, D.J. Smith, P.E.J. Flewitt, A.C.F. Cocks, On the evaluation of the Bauschinger effect in an austenitic stainless steel—The role of multi-scale residual stresses, *Int. J. Plast.* 84 (2016) 203–223, <https://doi.org/10.1016/j.ijplas.2016.05.009>.
- [68] X. Zhang, Y. He, S. Zhao, H. Ding, Y. Hu, Innovative liquid metal strategy for real-time thermal control in additive manufacturing, *J. Mater. Process. Technol.* 322 (2023) 118166, <https://doi.org/10.1016/j.jmatprotec.2023.118166>.
- [69] L.C. Wei, L.E. Ehrlich, M.J. Powell-Palm, C. Montgomery, J. Beuth, J.A. Malen, Thermal conductivity of metal powders for powder bed additive manufacturing, *Addit. Manuf.* 21 (2018) 201–208, <https://doi.org/10.1016/j.addma.2018.02.002>.
- [70] Y.Z. Sun, L. Zhang, F. Lin, X.Y. Liang, Research on temperature in floated powder bed fusion laser additive manufacturing process, *Electromachining & Mould* 4 (2024) 55–60, <https://doi.org/10.3969/j.issn.1009-279X.2024.04.009>.
- [71] H.R. Kotadia, G. Gibbons, A. Das, P.D. Howes, A review of Laser Powder Bed Fusion Additive Manufacturing of aluminium alloys: microstructure and properties, *Addit. Manuf.* 46 (2021) 102155, <https://doi.org/10.1016/j.addma.2021.102155>.